Master Thesis

Designing and testing an objective for imaging ultracold quantum gases

Thomas Öttl

September 16, 2019

Supervised by Univ.-Prof. Rudolf Grimm,
Dr. Emil Kirilov
Institut für Experimentalphysik

Contents

Abstract

This work documents the computer-aided design and experimental performance test of a microscope objective to image ultracold quantum gases. It also highlights an alternative approach to measure the wavefront error of optical systems, one which has received little attention in this particular field. The objective is with one exception made from off-the-shelve lenses and reaches a formidable resolution close to 1.6 microns and a diffraction limited field of view of 100 microns while also showing axial and lateral achromatic performance for two wavelengths 671 nm and 766 nm. Our goal is to improve an existing imaging system in an experiment investigating ultracold quantum gas mixtures of Lithium and Potassium.

1 Introduction

The development of optical instruments to magnify distant or small objects has rapidly improved the understanding of processes which could not be seen by the eye itself. The microscope, which was an improvement from the magnifying glass, was in particular helpful across many fields of sciences to enhance our ability to investigate the microscopic world. Robert Hooke was probably the most important contributor in developing a compound microscope in the 17th century similar to the ones used nowadays, with an objective and an eye piece [1]. Over centuries of development and exploration beyond optical microscopy, there are currently three main techniques that have further subdivisions: optical-, scanning probe- and electron microscopy. In optical microscopy visible light is used to image an object either by transmitting light through the sample or reflecting light off the sample. This method has a wide spread use in biology, medicine and physics to probe tissues or gases. Scanning probe microscopy is a technique that creates an image of a surface by scanning an area of interest with a sub millimeter sized probe. It is mostly used to manipulate surfaces on a nano scale, leading to nanolitography. In electron microscopy, electron beams are used to image an object of interest. This works quite similar to optical microscopy and has in principle a very significant advantage. One of the limiting factors on the resolution of an imaging system is the wavelength of the light or electrons respectively. While the visible regime is between roughly 400 and 700 nm, electrons can achieve shorter wavelengths at high velocities due to special relativity which leads to a higher resolution. It is however technically more difficult and more expensive to implement, hence optical microscopes are preferred if the resolution is sufficient. In the field of cold atoms, most laboratories use optical microscopes to investigate the properties of an atom cloud with the help of an imaging beam resonant to the atoms.

1.1 Imaging in quantum gas experiments

In quantum gas microscopy, both optical and electron microscopy have found applications. For optical microscopy, there are two different ways to image a quantum gas, namely absorption and fluorescence imaging. In absorption imaging, the intensity distribution of a light beam passing through the cloud of atoms is recorded on a detector and compared with the intensity without atoms in its path. In fluorescence imaging, the gas gets excited and fluorescence photons are collected. Fluorescence imaging is in general the preferred method for single-atom sensitivity in a lattice due to its higher signal-to-noise ratio. Absorption imaging is better suited for getting information about the whole cloud. Furthermore, one can distinguish between imaging a trapped, tightly confined gas, commonly known as in situ imaging and time-of-flight (TOF) imaging, where the gas gets released from the trap and expands in free space. These two methods allow studying different properties, as in situ is primarily used to get real space information such as the atomic density, density fluctuations and correlation functions, which need a higher resolution because of the high sample density compared to the TOF method. TOF imaging reveals the momentum distribution of the gas if the expansion is ballistic and is in general easier to realize than in situ imaging [2], from a technical point of view.

As an example for imaging in the field of cold atoms, a remarkable observation was made more than two decades ago as the first Bose-Einstein-condensate (BEC) [3], shown in Figure 1.1, was experimentally realized and eventually imaged with time-of-flight absorption imaging. While the imaging part itself or the method used didn't play a role in creating the BEC, the images eventually hold all the information which are crucial for investigating its properties. The images show an area, or field of view, of 200x270 μm hence a magnifying imaging system is imperative to obtain information.

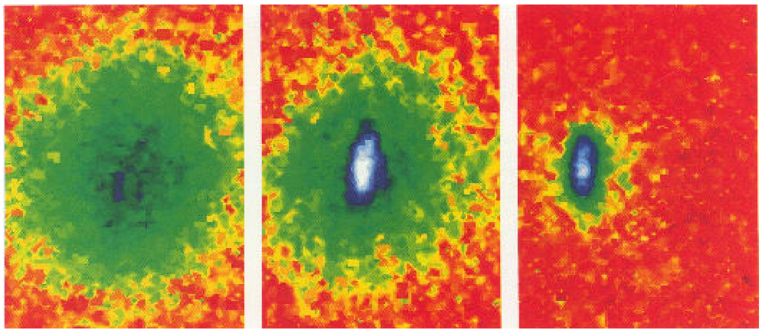

Figure 1.1: A false colour image of the velocity distribution of a Rubidium-87 cloud. The images from left to right show the formation of a BEC after several cooling stages in the center of the cloud. Image taken from [3].

1.2 High resolution imaging

In quantum gas microscopy, one of the technical problems to achieve high resolution is the accessibility of the sample. The ultrahigh vacuum chambers in quantum gas experiments typically feature thick glass walls in the order of several millimeters, limiting optical access for imaging system. This results in lower numerical aperture (NA) values, which directly affects the resolution limit, of the imaging system compared to other applications where no vacuum chambers are required. Workarounds to these problems have already been developed, such as placing optical elements inside the vacuum chamber or using solid immersion oils to increase the NA. Increasing the NA also means that the imaging depth of focus decreases.

In high NA systems (0.8), that depth is usually no more than a few micrometers. To achieve sharp images of a gas cloud, the samples depth along the optical axis should not exceed the imaging depth of focus, which is usually done by creating quasi 2D samples. These are experimentally realized by confining a sample of trapped atoms stronger along the optical axis than in the plane perpendicular to it. Such shallow samples can be created in various ways, for example with adding a 1D lattice as shown in Figure 1.2.

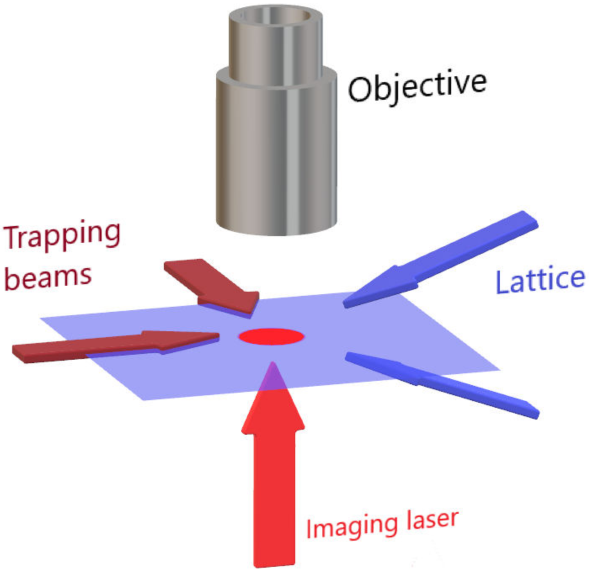

Figure 1.2: Schematic setup for preparing a 2D sample as its done by the Chin group in Chicago [2]. A trapped sample of atoms (red dot in the center) gets strong confinement in imaging direction from two lattice beams approaching from a small angle with respect to the trapping beams plane. The imaging beam, approaching from below, can then be used for absorption imaging. Image adapted from [2].

In high resolution absorption imaging, the imaging beam typically requires to be a short pulse of a few micro seconds with an intensity satisfying $I \gg I_s$, where I_s is the saturation intensity. This is necessary because the shallow depth of focus doesn't provide much room for atom displacement before getting kicked out the focus and the high intensity reduces effects from the scattered radiation fields on an atom imposed by other atoms. The atomic density can eventually be derived by a modified Lambert-Beer law for this 2D geometry [4]

$$n = \frac{1}{\sigma}\Big(ln\frac{I_0}{I_t} + \frac{I_0 - I_t}{I_s}\Big) \tag{1.1}$$

where σ is the radiative cross section of an atom, I_0 the intensity of the incident imaging beam and I_t the intensity after passing the sample. This formula can be used to convert intensity images to atomic density profiles, as shown in Figure 1.3 which can subsequently be used to derive quantities like equations of state, local density fluctuations, the density-density correlation function and the static structure factor [2] [4].

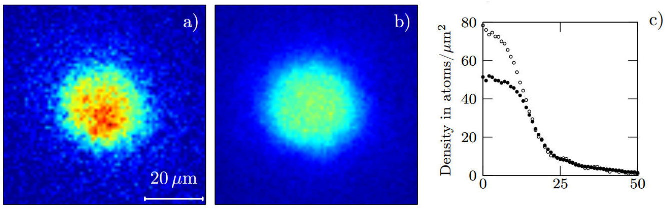

Figure 1.3: Absorption images of a 2D atomic sample. Images a) and b) differ mainly by the imaging beam strength $I/I_0 = 40$ for a) and $I/I_0 = 0.5$ for b). The radial density profile is shown in c), where the hollow circles refer to a) and the filled circles to b). Image taken from [4].

1.3 Quantum gas microscopes

The term quantum gas microscope refers to microscopes that feature up to single atom sensitivity by utilizing fluorescence instead of absorption imaging. They are mainly used to study condensed matter models, using quantum gases trapped in optical lattices [5]. The samples are typically created by preparing a 2D sample as discussed in the previous section and then loading the atoms in a 3D lattice. When the imaging resolution is smaller than the lattice constant, it is possible to identify single lattice sites in a single lattice plane [6]. A list of quantum gas microscopes known to the author is given in table 1.1.

Table 1.1: List of quantum gas microscopes around the world. The resolution is the given by the experimentally measured FWHM of point sources. The Erbium experiment in Harvard is in the planning phase to date.

Laboratory	Species	Resolution in nm	Reference
Harvard	^{87}Rb	600	[7]
Harvard	^{6}Li	520	[8]
Harvard	Er	-	-
Strathclyde	^{40}K	580	[9]
MIT	^{40}K	640	[10]
Toronto	^{40}K	600	[11]
MPQ	^{6}Li	900	[12]
MPQ	^{87}Rb	700	[13]
Kyoto	^{174}Yb	310	[14]
Tokyo	^{173}Yb	320	[15]

The single-site resolution features a way to study quantum correlation at the smallest possible scale. Bosonic quantum gases for example were used in quantum gas microscopy to study phase transitions from superfluid to the Mott insulating regime [16]. Shown in Figure 1.4, in situ fluorescence images are taken to determine the exact site occupation in the lattice. The known lattice geometry and the fluorescence signal of the atoms from in situ images are then used in an algorithm to precisely determine which spots are occupied. Further evaluation of the data concludes a probability of 94.9(7)% to spot an atom per site at $16E_r$. Having such precise determination of the occupation numbers allows a reliable experimental study of thermometry in the Mott state.

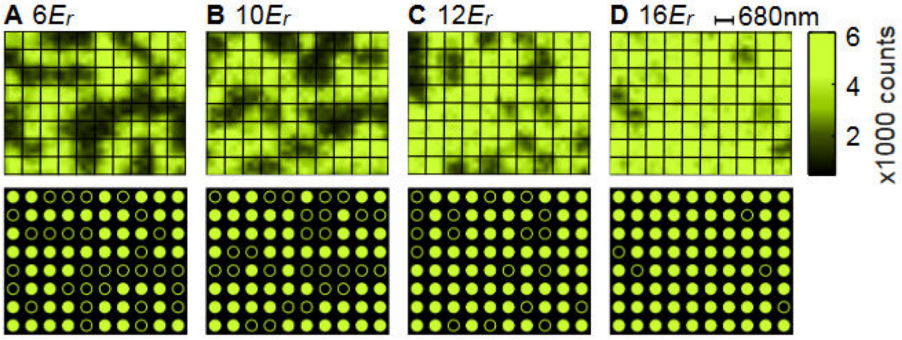

Figure 1.4: Single-site fluorescence imaging of a quantum gas transitioning from the superfluid regime A to a Mott insulator D, varying with lattice depth E_r. The top row shows the actual in situ images while in the middle row an algorithm is used to determine which individual lattice sites are occupied by an atom and which are empty. The lattice constant is 680 nm. Image taken from [16].

Further study in this field include phase transitions from a paramagnet to an antiferromagnet [17], strongly correlated dynamics in optical lattices [18] and string order in low-dimensional Mott insulators [19]. In fermionic systems, measurements so far included spin correlation functions [20] and in situ temperature and entropy measurements [13].

1.4 Outline of the thesis

This work documents the design and experimental testing of a microscope objective for imaging ultracold quantum gases. Its goal is to upgrade the current imaging system in the Fermionic Lithium (and Bosonic) Potassium experiment, or FeLi(Bo)Kx, in one of our labs. The experiment is set to investigate properties of quantum gas mixtures, Fermi-Fermi or Bose-Fermi gases, and was successful in creating one of the first heteronuclear Fermi-Fermi mixtures [21]. Over the past decade since its construction, imaging was done by a x4 magnification lens system, which was sufficient for its studies. In a recent publication about probing the interface of a phase-separated Bose-Fermi mixture, it is shown that the resolution of the current imaging system might soon reach its limit for further investigating the interplay between bosons and fermions in such mixtures. As shown in Figure 1.5, a small BEC of ^{41}K atoms is submerged in a Fermi sea of ^{6}Li atoms. Given the detector pixel size of 6.8 μm, the BEC in this cloud is roughly two pixels wide. This makes for example the investigation of the spatial overlap between both regions, which is even smaller, nearly impossible as much of vital information would be hiding in a single pixel.

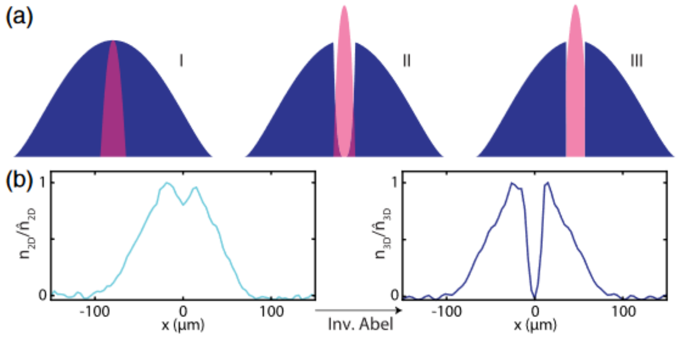

Figure 1.5: a) Density profiles from left to right at increasingly repulsive interaction between both species. Eventually at stage III the components are phase separated. b) Left: Experimentally measured density for a slice of the Fermi sea. Right: The inverse Abel transform reveals the real radial density profile for the gas cloud. Image taken from [22].

The example given in Figure 1.5 is just one of the reasons to upgrade the current imaging system. Throughout this work, the reader is introduced to principles of optical systems and wave optics of image formation in chapter 2. Classical aberrations and their description in terms of wavefront errors are discussed in section 2.5. A method for optical phase retrieval by nonlinear optimization, first introduced by James R. Fienup and Gregory R. Brady in [23], was applied to quantify the objective's performance. The code for such an algorithm was written by Mirsolaw Marszalek [24] and was used with little modification as the author proposed it. The phase retrieval algorithm is described in 2.7. Chapter 3 and 4 describe the design process of the objective and the experimental testing of its performance. In section 4.4 the experimental values are compared to the predicted ones by the design simulation. Eventually a summary and outlook is given in chapter 5.

2 Optical systems and their properties

This chapter lays the groundwork to understand the imaging process in terms of wave optics. The concept of stops and pupils in optical systems is introduced and then the reader is guided through the image formation theory described by wave optics. Aberrations are presented in their classical appearance and then described in terms of wavefront aberrations. Furthermore, the problem of retrieving an unknown phase from intensity measurements is discussed and it is shown how solving this particular problem helps to analyze the performance of an imaging system. At the end, some quality evaluation techniques are discussed.

2.1 Aperture stop and numerical aperture

Optical systems can only collect a limited amount of light depending on the diameter of the optical elements. The amount of light accepted can further be adjusted by adding an aperture stop. The aperture stop is typically an iris diaphragm and it plays an major role in optical systems, as it allows control of illumination and spherical aberrations. An illustration of the aperture stop in an optical system is shown in Figure 2.1.

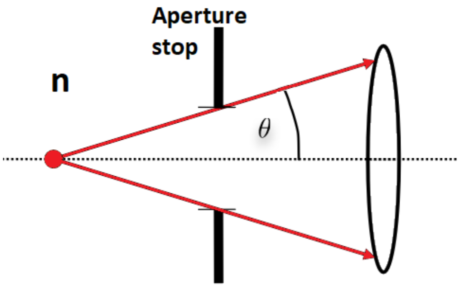

Figure 2.1: A point source is placed along the optical axis of a setup consisting of an aperture stop followed by a lens. The aperture stop is limiting the amount of light that is accepted into the following optical system. From the maximum angle of a light ray that passes through the stop, the numerical aperture NA is defined.

Such an aperture stop can be placed before, after or embedded within an optical system depending on the design. If no separate stop is present, then the amount of light accepted by a system is simply limited by the lens diameters. Therefore, the aperture stop can be defined precisely as the aperture that physically limits the accepted angle of incident rays the most [25].

Consider a point source along the optical axis illuminating light isotropically, then one can define a mathematical quantity derived from the angle subtended from the point source to the rim of the physical aperture stop θ, known as the numerical aperture NA

$$NA = n \cdot sin(\theta). \tag{2.1}$$

In this definition, n is the refractive index of the medium between the point source and the optical system. This means that the numerical aperture is conserved if rays go through flat refractive interfaces, as in Snell's law. This becomes important when imaging through materials with n≠1, like glass or solid immersion oils. The numerical aperture can be defined on both sides of the system, with respect to the object and the image plane. For an optical system with some magnification M, the numerical aperture in object space NA_o and image space NA_i uphold the relation

$$NA_i = |M| NA_o. \tag{2.2}$$

2.2 Entrance and exit pupil

The concept of entrance and exit pupils is particularly helpful for describing more complex optical systems. They are defined as the images of the aperture stop depending on from which side one looks through the system. For example in Figure 2.1, there are no imaging elements between stop and object plane, which means that the stop is also the entrance pupil. The same concept applies for a stop after a lens, where the exit pupil would coincide with the physical stop, when observed from the image plane. However, it gets more challenging in a system with multiple lenses when the stop is embedded inside the optical apparatus. Such a case is considered with two lenses in Figure 2.2.

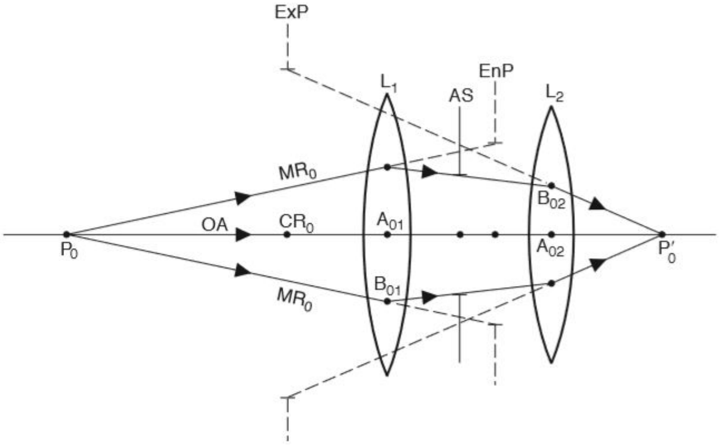

Figure 2.2: An optical system with two lenses at L$_1$ and L$_2$ and a physical aperture stop (AS) inbetween. The entrance (EnP) and exit (ExP) pupil are images of the stop with respect to the observation point P$_0$ or P$_0'$. Image taken from [26]

When looking from the object side P_0, one would not see the aperture itself but the image of the stop through the elements between observer and the physical stop. The same applies to the exit pupil, when the observer is located at $P_0{}'$ then the exit pupil is the image of the stop imaged through the elements between stop and image plane. As shown in Figure 2.2, when a point source illuminates light isotropically, the maximum angle where light rays are still accepted by the aperture stop are called marginal rays. The numerical aperture is defined with respect to these rays. A hypothetical extension of these rays through the first lens, indicated by dashed lines, leads to the entrance pupil. The exit pupil is found the same way from the image points perspective. The exit pupil has an important meaning in image processing, because as it will be seen later diffraction formulas will be used with respect to the exit pupil and also the resolution limit is tied to the exit pupil radius [25] [26].

2.3 Diffraction theory

In this section the Fresnel- and Fraunhofer approximations are derived from the Huygens-Fresnel principle, which are very useful to describe the diffraction phenomenon. The Huygens-Fresnel principle itself arises from the Rayleigh-Sommerfeld diffraction theory which is not discussed here, the reader is referred to [27]. A few mathematical basics are briefly introduced to then go on with image formation theory and phase retrieval.

Consider a monochromatic wave

$$u(x,t) = A(x)cos(2\pi\nu t + \Phi(x)) \tag{2.3}$$

with some amplitude $A(x)$, a Phase $\Phi(x)$ and ν being the frequency. Optical waves must obey the scalar wave equation for every source free point

$$\nabla^2 u - \frac{n^2}{c^2}\frac{\partial^2 u}{\partial t^2} = 0, \tag{2.4}$$

with the refractive index n and c is the speed of light in vacuum. It follows from equation (2.3) and (2.4) that $u(x,t)$ has to satisfy the Helmholtz equation

$$(\nabla^2 + k^2)u = 0 \tag{2.5}$$

with $k = \frac{2\pi}{\lambda}$. Throughout this work, monochromatic waves propagating through space are considered to obey the Helmholtz equation.

2.3.1 Huygens-Fresnel principle

Consider an aperture in the ξ, η plane illuminated by monochromatic light, as shown in Figure 2.3. The diffracted wave in the observation plane can be described by the Huygens-Fresnel principle [27]

$$U(P_0) = \frac{1}{i\lambda} \iint_{\Sigma} U(P_1) \frac{e^{ik\vec{r_{01}}}}{|r_{01}|} cos(\theta) ds \tag{2.6}$$

where vector $\vec{r_{01}}$ is pointing from P_0 to P_1. The angle θ is between $\vec{r_{01}}$ and the normal vector $\vec{n}$ orthogonal to the pupil plane. This mathematical formula can be physically interpreted as the field $U(P_0)$ in the observation plane is consisting of a superposition of diverging spherical waves which come from every other point within the aperture. In rectangular coordinates and using the cosine definition $cos(\theta) = \frac{z}{r_{01}}$, a more convenient form is

$$U(x, y) = \frac{z}{i\lambda} \iint_{\Sigma} U(\xi, \eta) \frac{e^{ikr}}{r_{01}^2} d\xi d\eta. \tag{2.7}$$

The length of the vector $\vec{r_{01}}$ known to be

$$|r_{01}| = \sqrt{z^2 + (x - \xi)^2 + (y - \eta)^2}. \tag{2.8}$$

These expressions already uses two approximations. It is assumed that the light field is a scalar field and $r_{01} \gg \lambda$ is upholding.

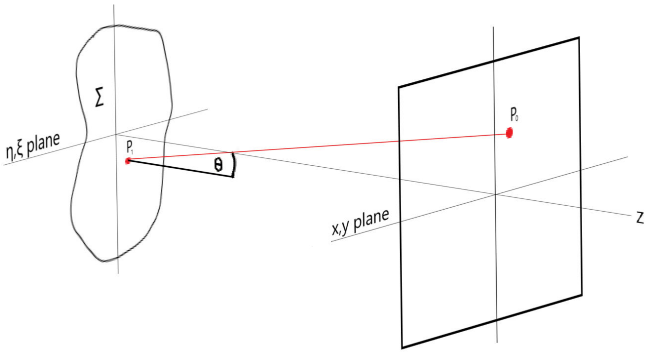

Figure 2.3: Conceptual diffraction geometry. A light source illuminating the η, ξ plane from the left and the diffracted light field in the x, y plane.

Fresnel approximation

The Huygens-Fresnel principle according to equation (2.7) can be simplified for the near field by approximating the $|r_{01}|$ according to

$$\sqrt{1 + b} = 1 + \frac{1}{2}b - \frac{1}{8}b + ... \tag{2.9}$$

where b is a small quantity. Applying the first two terms to equation (2.8) with $b = (x - \xi)^2 + (y - \eta)^2$ one gets

$$r_{01} \approx z \left(1 + \frac{1}{2}\left(\frac{x - \xi}{z}\right)^2 + \frac{1}{2}\left(\frac{y - \eta}{z}\right)^2\right) \tag{2.10}$$

and the field in the image plane can be expressed as

$$U(x,y) = \frac{e^{ikz}}{i\lambda z} \iint_{-\infty}^{\infty} U(\xi,\eta) e^{i\frac{k}{2z}((x-\xi)^2+(y-\eta)^2)} d\xi d\eta. \tag{2.11}$$

Expressing the exponent in equation (2.11) in a different way, it is easier to see that this is a Fourier transform of the product of the aperture distribution $U(\xi,\eta)$ and a quadratic phase function

$$U(x,y) = \frac{e^{ikz}}{i\lambda z} e^{\frac{ik}{2z}(x^2+y^2)} \iint_{-\infty}^{\infty} \Big\{ U(\xi,\eta) e^{i\frac{k}{2z}(\xi^2+\eta^2)} \Big\} e^{-\frac{-ik}{2z}(x\xi+y\eta)} d\xi d\eta, \tag{2.12}$$

which is commonly referred to as Fresnel diffraction integral. This approximation holds true as long as the observation plane is close to the diffracting aperture. An important note is that the spherical wave which travels from the aperture to the observation plane is given by a quadratic phase exponential. For a wave travelling along positive z-axis the phase exponential represents a diverging spherical wave if it has a positive sign $e^{\frac{ik}{2z}(x^2+y^2)}$, while for a converging spherical wave the sign requires to be negative $e^{-\frac{ik}{2z}(x^2+y^2)}$. In the case of waves travelling along negative z-axis, the signs need to be the opposit. [27].

Fraunhofer approximation

Another important approximation can be made in regard to the far field

$$z \gg \frac{k(\xi^2+\eta^2)_{max}}{2}. \tag{2.13}$$

If in addition to the assumptions of the Fresnel approximation also the far field approximation holds, then we get the result from equation (2.12) but with the quadratic phase $e^{-\frac{ik}{2z}(\xi^2+\eta^2)}$ converging to

$$U(x,y) = \frac{e^{ikz}}{i\lambda z} e^{\frac{ik}{2z}(x^2+y^2)} \iint_{-\infty}^{\infty} U(\xi,\eta) e^{-\frac{-i2\pi}{\lambda z}(x\xi+y\eta)} d\xi d\eta. \tag{2.14}$$

This is convenient because the field in the observation plane can be retrieved by a simple Fourier transformation of the aperture distribution. The Fourier transform in equation (2.14) can then be evaluated at frequencies $f_X = x/\lambda z$, $f_Y = y/\lambda z$ [27].

2.3.2 Diffraction pattern for circular aperture

For experimental application, the intensity is the measurable quantity of an optical field, therefore we are now eager to find the intensity distribution of diffracted light by a small aperture. If we consider a circular aperture of radius w, then the amplitude transmittance of such an aperture t_A can be described by

$$t_A(q) = circ\Big(\frac{q}{w}\Big), \tag{2.15}$$

where $circ(\frac{q}{w})$ is the circle function, a function with circular symmetry that is 1 inside of w and 0 outside, and q denoting the radial coordinate of the aperture. The circular symmetry allows us to use the Fourier-Bessel transform $B\{\}$ to substitute the two dimensional Fourier transform in the Fraunhofer approximation in equation (2.14)

$$U(r) = \frac{e^{ikz}}{i\lambda z} e^{\frac{ik}{2z}(r^2)} B\{U(q)\}\bigg|_{\rho=\frac{r}{\lambda z}} , \tag{2.16}$$

with r denoting the image plane coordinate and $\rho = \sqrt{f_x^2 + f_y^2}$ is the radius in spatial frequency domain. Under the assumption of unit amplitude illumination with an orthogonal incident wave vector, the aperture field distribution $U(q)$ can be replaced with the amplitude transmittance $t_A(q)$. The Fourier-Bessel transform of a circular function has a known solution [27]

$$B\Big\{circ\Big(\frac{q}{w}\Big)\Big\} = A\frac{J_1(2\pi w\rho)}{\pi w\rho}, \tag{2.17}$$

where $A = \pi w^2$ is the area of the aperture and J_1 is a first order Bessel function of the first kind. Using the result in equation (2.17) in (2.16) and applying the modulus square, we arrive at the intensity distribution $I(r)$

$$I(r) \equiv |U(r)|^2 = \Big(\frac{1}{\lambda z}\Big)^2 A\Big(2\frac{J_1(kwr/z)}{kwr/z}\Big)^2 \tag{2.18}$$

The result in equation (2.18) is also commonly known as Airy pattern or Airy disk and is shown in Figure 2.4. The first minimum in this pattern occurs at r_0=1.22, hence the relation

$$r_0 = 1.22\frac{\lambda z}{w} \tag{2.19}$$

defines the radius of the center peak, which also defines the resolution limit or Rayleigh criterion in optical systems. This means that two peaks have to be at least a distance of r_0 apart in order to be resolvable by common means.

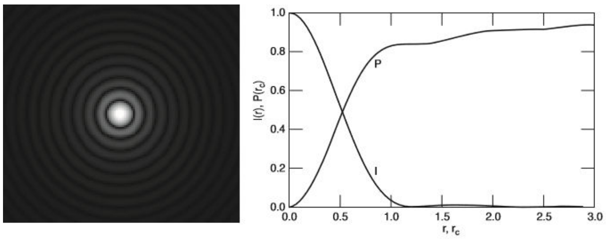

Figure 2.4: Left: View of an ideal airy pattern observed from the aperture. Right: Intensity distribution I in the airy pattern as a function of distance r from the center center peak. The total power $P(r_c) = 1 - J_0^2(\pi r_c) - J_1^2(\pi r_c)$ inside a circle area of radius r_c is also shown. Image taken from [28].

2.3.3 Thin lens properties

Lenses are key components of optical systems which are used to focus, collimate or diverge light. As they are made of transparent materials with some refractive index larger than the one in air, the light wave is slower when propagating through lenses than through air. A thin lens is considered to be one where every point on the incident wave is assumed to leave in approximately the same spatial coordinate mirrored to the opposite side of the lens [27].

Considering a thin lens with refractive index n, a thickness Δ_0 at the center and a position dependent thickness $\Delta(x, y)$. The total phase delay $\Phi(x, y)$ imposed on a wave traveling through lenses is given by

$$\Phi(x, y) = kn\Delta(x, y) + k(\Delta_0 - \Delta(x, y)), \tag{2.20}$$

with $kn\Delta(x, y)$ being the phase delay caused by the lens material and because the wave has to travel through air for longer on the rim of lens than in the center, it is imposing another phase delay characterized by $k(\Delta_0 - \Delta(x, y))$. Illustrating this by Figure 2.5 a), a point in the wavefront hitting the center of this lens will see the thickest part of the lens, so it will sustain a longer phase delay than a point going through the edge of the lens. This can as well be written as a phase transformation

$$t_l(x, y) = e^{ik\Delta_0} e^{ik(n-1)\Delta(x,y)} \tag{2.21}$$

and the field before the lens $U_l(x, y)$ and after the lens $U_l'(x, y)$ are connected via relation

$$U_l'(x, y) = t_l(x, y) U_l(x, y). \tag{2.22}$$

The thickness function $\Delta(x, y)$ depends on the shape of the lens. For most common simple lenses, a thickness function can be derived by geometrical means as shown in Figure 2.5.

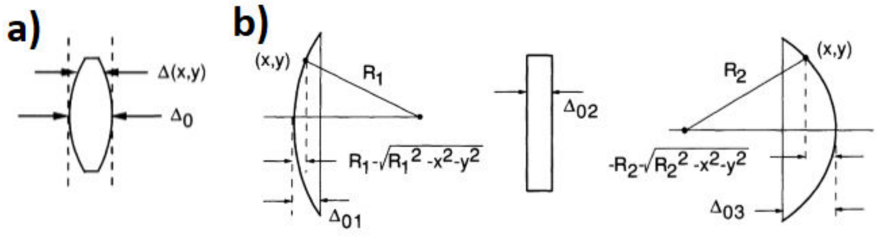

Figure 2.5: a) A thin lens with some thickness function $\Delta(x, y)$. b) The lens split into 3 parts to derive the thickness function. Figure modified from [27].

Without going into detail of the geometry, one can derive the thickness function as

$$\Delta(x, y) = \Delta_0 - R_1 \left(1 - \sqrt{1 - \frac{x^2 + y^2}{R_1^2}}\right) + R_2 \left(1 - \sqrt{1 - \frac{x^2 + y^2}{R_2^2}}\right), \tag{2.23}$$

with $\Delta_0 = \Delta_{01} + \Delta_{02} + \Delta_{03}$ according to Figure 2.5. While the thickness function is complete in that form, it can be simplified by only taking rays near the optical axis into account. Hence, x and y are small, and we can use the Taylor approximation to expand the roots in equations (2.23)

$$\sqrt{1 - \frac{x^2 + y^2}{R_{1,2}^2}} \approx 1 - \frac{x^2 + y^2}{2R_{1,2}^2} \tag{2.24}$$

Ultimately, the thickness function within the paraxial approximation is given by

$$\Delta(x, y) = \Delta_0 - \frac{x^2 + y^2}{2} \left(\frac{1}{R_1} - \frac{1}{R_2} \right). \tag{2.25}$$

With the thickness function known, the phase transformation in equation (2.22) may be written as

$$t_l(x, y) = e^{-\frac{ik}{2f}(x^2+y^2)} \tag{2.26}$$

where $f := [(n-1)(\frac{1}{R_1} - \frac{1}{R_2})]^{-1}$ is the focal length of the lens. The constant phase $e^{ikn\Delta_0}$ in equation (2.22) is neglected since it is position independent. The result in equation (2.26) is quite useful for calculating the exit field of a lens for a given incident wave for a whole variety of lens geometries. As an example, considering a biconvex lens as in figure 2.5 a), if the incident wave is a plane wave then the result is simply the result of equation (2.26)

$$U_l'(x, y) = e^{-\frac{ik}{2f}(x^2+y^2)} \tag{2.27}$$

which is in a physical context a converging spherical wave that focuses at the focal distance f which is positive for this lens.

2.4 Image formation

As the previous section has shown how lenses translate light fields, the focus in now on how an object is imaged through a lens. Restrictions are kept to a thin aberration free lens illuminated with monochromatic light. A simple imaging setup is shown in Figure 2.6, where a planar object represented by a field $U_0(\xi, \eta)$ is placed at a distance z_1 before a lens and its image $U_i(u, v)$ is formed at z_2 after the lens [27]. The field in the image plane is given by

$$U_i(u, v) = \iint_{-\infty}^{\infty} h(u, v, \xi, \eta) U_0(\xi, \eta) d\xi d\eta, \tag{2.28}$$

with the point spread function (PSF) $h(u, v, \xi, \eta)$. The PSF

$$h(u, v, \xi, \eta) \approx K\delta(u \pm M\xi, v \pm M\eta) \tag{2.29}$$

is the field amplitude at the image plane generated by a point source in the object plane, which is why it is assumed to be a delta function. Furthermore, K denotes a complex constant and M is the magnification of the system.

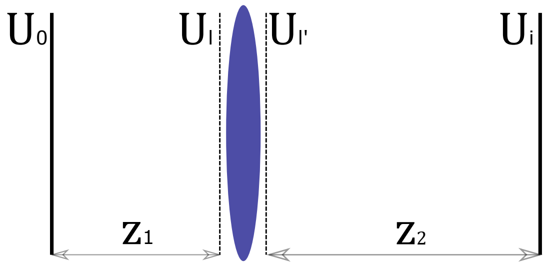

Figure 2.6: Schematic imaging setup in a nutshell, with an object plane U_0 in distance z_1 from a lens and the image plane U_i at a distance z_2. Light propagation follows by convention from left to right.

Once the point spread function is found, the imaging system can be fully described. Under the assumption of an illuminating point source in the object plane, we would expect spherical light waves being emitted, diverging towards the lens plane U_l

$$U_l(x,y) = \frac{1}{i\lambda z_1} e^{\frac{ik}{2z_1}((x-\xi)^2+(y-\eta)^2)}. \tag{2.30}$$

The field U_l' on the right side of the lens is calculated by using equation (2.22)

$$U_l'(x,y) = U_l(x,y)P(x,y)e^{-\frac{ik}{2f}(x^2+y^2)}. \tag{2.31}$$

The function $P(x,y)$ is called pupil function and is simply a geometric constraint that ensures the field is zero outside the pupil. The pupil function is 1 inside of the lens and 0 elsewhere. The exit field can now be propagated to the image plane by using Fresnel diffraction according to equation (2.12) and ignoring constant phase shifts

$$h(u,v,\xi,\eta) = \frac{1}{i\lambda z_2} \iint_{-\infty}^{\infty} U_l' x, y e^{\frac{ik}{2z_2}((u-x)^2+(v-y)^2)} dxdy \tag{2.32}$$

which provides a rather inconvenient expression

$$\begin{aligned} h(u,v,\xi,\eta) = {} & \frac{1}{\lambda^2 z_1 z_2} e^{\frac{ik}{2z_2}(u^2+v^2)} e^{\frac{ik}{2z_1}(\xi^2+\eta^2)} \\ & \iint_{-\infty}^{\infty} P(x,y) e^{\frac{ik}{2}(\frac{1}{z1}+\frac{1}{z_2}-\frac{1}{f})(x^2+y^2)} e^{-ik((\frac{\xi}{z_1}+\frac{u}{z_2})x+(\frac{u}{z_1}+\frac{v}{z_2})y)} dxdy. \end{aligned} \tag{2.33}$$

With equations (2.28) and (2.33), a relation between object and image can be established. However, there are a few more simplifications that can be made to the latest expression. One may notice the term $\frac{1}{z_1} + \frac{1}{z_2} - \frac{1}{f}$ in one of the exponents, which has to be exactly zero according to geometrical optics and is also known as the lens law

$$\frac{1}{z_1} + \frac{1}{z_2} - \frac{1}{f} = 0 \tag{2.34}$$

if z_2 is chosen to be the image plane. This has the quite obvious consequence, that we cannot calculate the field in defocused planes anymore. Next, the quadratic phase factor $e^{\frac{ik}{2z_2}(u^2+v^2)}$ can be neglected because the phase field in the image plane is not of interest. The phase term $e^{\frac{ik}{2z_1}(\xi^2+\eta^2)}$ can also be neglected when considering that the response to a point in the object space spreads just over a small region in the image space. In this case, the phase term can be replaced by a phase that depends on image coordinates $e^{\frac{ik}{2z_1}\frac{u^2+v^2}{M^2}}$ where $M = -\frac{z_2}{z_1}$ is the magnification of the system. This term, now depending on image coordinates, can be neglected again because only the intensity in image space is of interest. The argument for dropping the latter phase term is rather crude here as it would otherwise require a lengthy discussion. For a thorough explanation the reader is referred to [29].

Applying these approximations, equation 2.33 is simplified to

$$h(u, v; \xi, \eta) \approx \frac{1}{\lambda^2 z_1 z_2} \iint_{-\infty}^{\infty} P(x, y) e^{-\frac{i2\pi}{\lambda z_2}((u-M\xi)x+(v-M\eta)y)} dxdy. \tag{2.35}$$

This gives an important result, as the impulse response can be found via Fraunhofer diffraction with an additional factor of $\frac{1}{\lambda z_1}$.

2.4.1 Object-image relation

With the impulse response known, the relation between object and image can be stated in a convenient form by introducing normalized coordinates $\tilde{\xi} = M\xi$ and $\tilde{\eta} = M\eta$, so the point spread function (2.35) revises to

$$h(u, v; \tilde{\xi}, \tilde{\eta}) \approx \frac{1}{\lambda^2 z_1 z_2} \iint_{-\infty}^{\infty} P(x, y) e^{-\frac{i2\pi}{\lambda z_2}((u-\tilde{\xi})x+(v-\tilde{\eta})y)} dxdy. \tag{2.36}$$

and with another set of normalized coordinates $\tilde{x} = \frac{x}{\lambda z_2}$, $\tilde{y} = \frac{y}{\lambda z_2}$, $\tilde{h} = \frac{1}{|M|}h$ we can write the relation from equation 2.28 as

$$U_i(u, v) = \iint_{-\infty}^{\infty} \tilde{h}(u - \tilde{\xi}, v - \tilde{\eta}) \Big[\frac{1}{|M|} U_0\Big(\frac{\tilde{\xi}}{M}, \frac{\tilde{\eta}}{M}\Big)\Big] d\tilde{\xi} d\tilde{\eta}, \tag{2.37}$$

where $U_0(\xi, \eta) = \frac{1}{|M|} U_0(\frac{\tilde{\xi}}{M}, \frac{\tilde{\eta}}{M})$ is the image definition from geometrical optics and

$$\tilde{h}(u, v) = \iint_{-\infty}^{\infty} P(\lambda z_2 \tilde{x}, \lambda z_2 \tilde{y}) e^{-i2\pi(u\tilde{x}+v\tilde{y})} d\tilde{x} d\tilde{y} \tag{2.38}$$

is the PSF according to diffraction theory. The important property that has been shown is that the image of an object is the convolution of the ideal image according to geometrical optics and the Fraunhofer diffraction associated to the lens aperture $U_i(u, v) = \tilde{h}(u, v) \circledast U(u, v)$ [27], $\circledast$ denoting the convolution operation.

2.5 Aberrations in general

The last sections dealt with thin, aberration free lenses. However, in a realistic optical setup the effect of aberrations have to be taken into account. Aberrations lower the performance of an optical system, but as it will be seen there is a certain threshold where aberrations are considered acceptable. This section will discuss defocus and the five Seidel aberrations [25].

Defocus

While defocus is technically not an aberration, it is still an error source when the image plane is not set properly. Consider a bundle of rays travelling through a lens as shown in figure 2.7. The cross sections tell the devastating effect when the image plane is out of focus. In the focus, the rays would ideally converge to a point, but as raytracing was done with a real lens it is spread over a finite area.

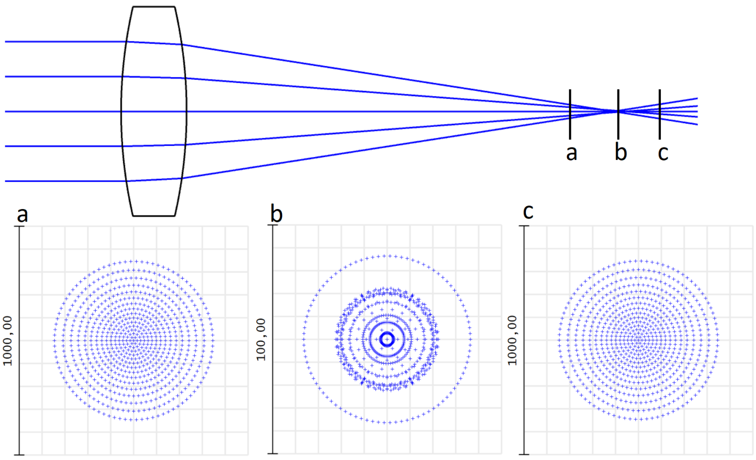

Figure 2.7: Top: Rays travelling through a lens from the left and intersecting at the paraxial focal plane b. Bottom: Cross sections of three planes showing the ray distribution around the optical axis.

Spherical aberration

Consider the same case as in 2.7, but this time the lens features larger spherical aberrations due to a bigger aperture stop diameter. The rays entering the lens at the rim intersect further on the optical axis than the rays close to the center. There is merely a spot where the rays are closest to one another, sometimes called as the circle of least confusion. Spherical aberrations are present in every lens and there is no way to completely remove them, however, there are tricks to decrease their magnitude in multi element systems, as it will be seen in chapter 3. The effect of spherical aberration is shown in Figure 2.8.

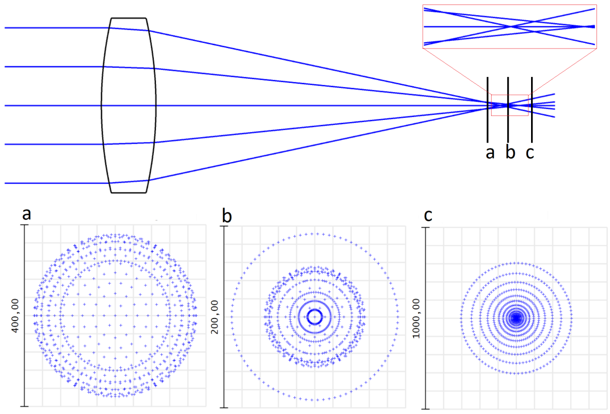

Figure 2.8: Top: Rays travelling through a lens with spherical aberration from the left and intersecting at different planes. Bottom: Cross sections of three imaging planes showing the ray distribution depending on the distance from the lens. The smallest spot diameter, or circle of least confusion, is at plane b.

Coma

To illustrate the effect of coma, consider an aberration free lens and let the incident wave be tilted as seen in Figure 2.9. Opposed to spherical aberrations, coma only occurs when rays approach off axis.

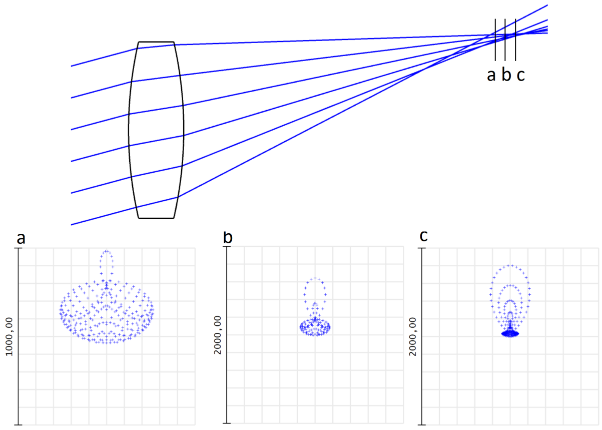

Figure 2.9: Top: Rays coming from an angle through the aperture and propagating through the lens. Bottom: Cross section of the rays in various spots around the circle of least confusion.

Similar to spherical aberrations, the ray pairs closer to the axis have a different focus spot than the rays hitting the rim of the lens. The cross section plots also show that coma is not a symmetrical aberration like spherical aberrations, but rather has a cone shape. Coma happens because the magnification depends on the size of the object height, which cannot be seen in the paraxial approximation since it is a non paraxial problem. Rays going through the center are imaged at different heights copmared to those going through the rim.

Astigmatism

Probably the most complex aberration to illustrate is astigmatism, hence it is shown in a 3D sketch in Figure 2.10.

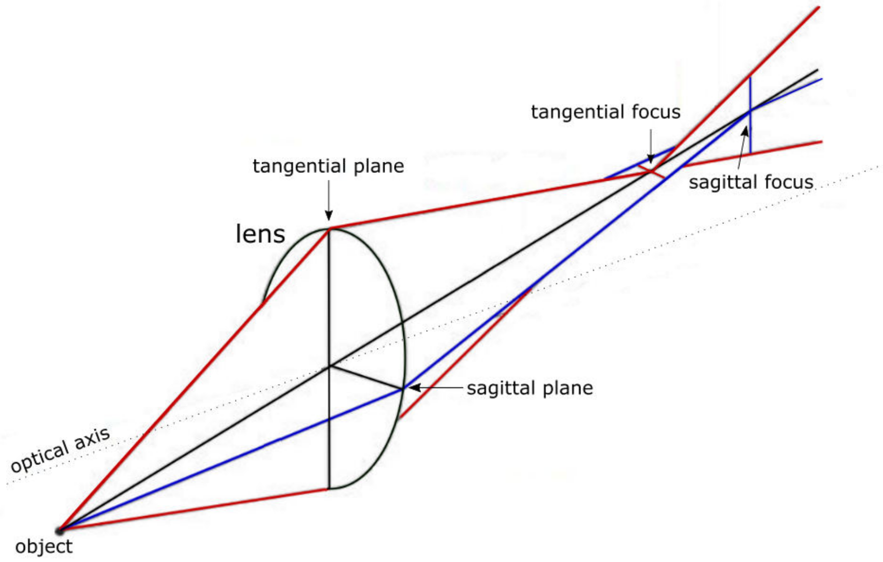

Figure 2.10: Schematic drawing of astigmatism. The marginal rays from an off-axis point source intersect at different focus points. Image adapted from [25].

Astigmatism is illustrated with respect to an object point that is off the optical axis. Now take two marginal ray bundles where one goes through the tangential plane and the other ray bundle goes through the sagittal plane. These two bundles do not focus at the same point because the source is off axis and therefore the magnification changes for different points in the field, just like for coma.

Field curvature and distortion

Field curvature and distortion are off axis aberrations that shift the location of image points without having an impact on the quality. Both are presented in figure 2.11. Considering both effects independently of each other, field curvature occurs when the angle of the incident rays increases with respect to the axis, so the paraxial focus plane is bending, which is equivalent to a curved image surface. While the rays still focus on a point that lies on the chief ray, this point is not on the paraxial plane indicated by the dotted line in figure 2.11a). Since detectors are usually flat, field curvature will always be present for off axis points. If only distortion is considered, as shown in Figure 2.11 b), all the rays form a good precise spot on the image plane, but it is radially displaced from the chief ray. This displacement as well increases with an increased angle of the incident rays hitting the lens. As Distortion scales with the cube of the image height, it shows most in the edges of the image, in particular the corners, to be displaced with respect to more centered points.

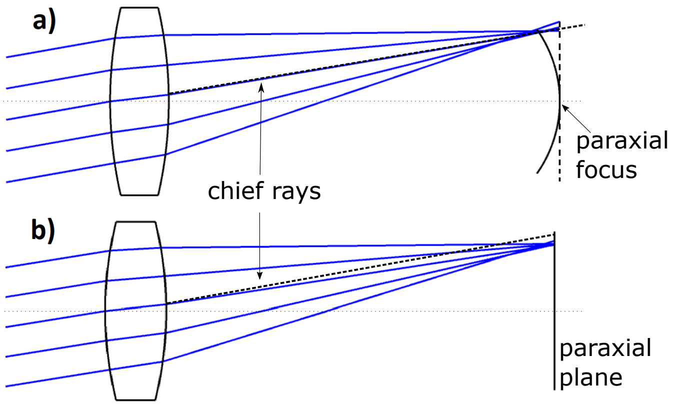

Figure 2.11: Illustrations of a) field curvature and b) distortion. The plane introduced by field curvature is also known as the Petzval curvature, is the surface where off axis points are focused. On a flat image plane, as indicated by the dashed line, points further from the optical axis are increasingly defocused. Distortion occurs when off-axis points are closer (barrel distortion) or further (pincushion distortion) away from optical axis. The dashed line indicates where the paraxial approximation predicts the focus on the chief ray position, but the actual position is displaced.

2.6 Wavefront aberrations

To describe aberration properly by wave optics, consider a point source emitting light rays isotropically according to Figure 2.12. Each of these rays has a optical path length $OPL = length \cdot n$ consisting of it's length times the refractive index of the medium it's propagating through. The OPL can be seen as the radius of the sphere emerging from the point source. All these rays have the same phase since they have the same origin, but this property breaks when it interacts with a real optical system. In the ideal case of an aberration free system, the wavefront which is emitted at the exit pupil would converge to a finite point in the image plane according to diffraction theory.

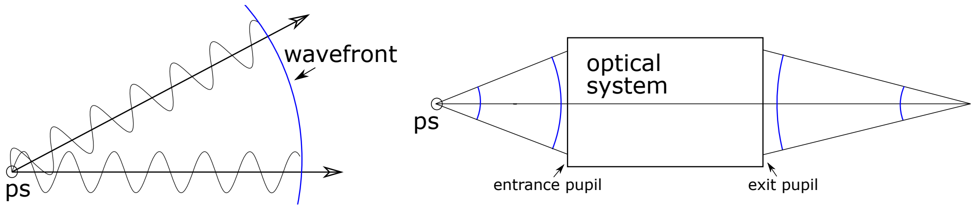

Figure 2.12: Left: The concept of a wavefront illustrated with light rays. At its surface the rays have the same phase, if they emerge from the same point source (ps). Right: An ideal imaging system where the wavefront from a point source PS diverges towards the entrance pupil and forms an ideal spherical wavefront at the exit pupil converging towards the image point.

However, even in well corrected system, imperfections in lenses lead to a deformation of the wave front, such that it no longer is spherical. Like shown in Figure 2.13, points on the real wavefront differ from the ones on the ideal one which is described by the optical path difference W.

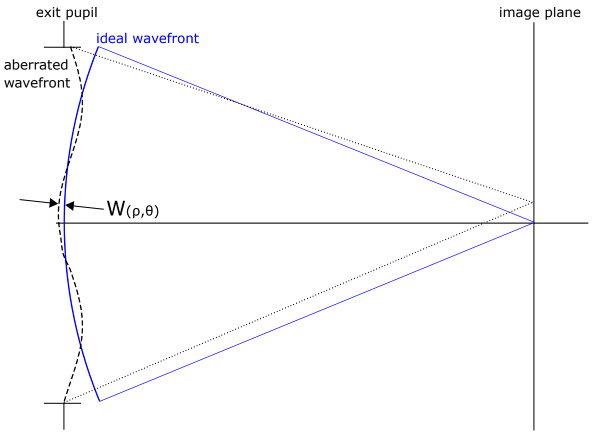

Figure 2.13: Illustration of an aberrated wavefront (dashed line) compared to the ideal reference wavefront. The optical path difference or wavefront error W is the path difference between a point on the ideal wavefront and the same point on the real, aberrated wavefront. Depending on the error sources it may change the lateral and axial focus point, spot geometry or simply broaden the image spot.

To describe the aberrated wavefront, typically a series of polynomials is used. This allows a precise investigation since each polynomial can be defined such that each one fits a certain type of aberration. Zernike polynomials are one way of describing the aberrated wavefront. They form a complete set of orthogonal polynomials over the unit circle which corresponds to the exit pupil plane. For a rotationally symmetric exit pupil, one can define an aberration function $W(\rho, \theta)$ as an expansion of orthonormal Zernike circle polynomials $Z_n^m(\rho, \theta)$ [26]

$$W(\rho, \theta) = \sum_{n=0}^{\infty} \sum_{m=0}^{n} = c_{n,m} Z_n^m(\rho, \theta) \tag{2.39}$$

with $0 \leq \rho \leq 1$ and $0 \leq \theta \leq 2\pi$. The indices n, m correspond to radial degree and azimuthal frequency. The coefficients $c_n m$ are defined as

$$c_{nm} = \frac{1}{\pi} \int_0^{2\pi} \int_0^{2\pi} W(\rho, \theta) Z_n^m(\rho, \theta) \rho d\rho d\theta \tag{2.40}$$

because of the orthogonality of $Z_n^m(\rho, \theta)$. This allows to express the mean and mean square of the aberration function to be expressed as

$$\langle W(\rho, \theta) \rangle = c_{00} \tag{2.41}$$

and

$$\langle W^2(\rho,\theta)\rangle = \sum_{n=0}^{\infty}\sum_{m=0}^{n} c_{nm}^2. \tag{2.42}$$

This leads to the particular quantity of interest, the root-mean-square of the wavefront error W_{rms}

$$W_{rms} = \sqrt{\langle W^2(\rho,\theta)\rangle - \langle W(\rho,\theta)\rangle^2} = \sqrt{\sum_{n=1}^{\infty}\sum_{m=0}^{n} c_{nm}^2} \tag{2.43}$$

Some polynomials are given as an example in table 2.1. In general, polynomials independent of θ describe sphercial aberration, where $\cos\theta$ terms correspond to coma and $\cos 2\theta$ terms to astigmatism.

Table 2.1: List of the first 13 Zernike circle polynomials $Z_j(\rho,\theta)$ where j denotes the polynomial number corresponding to some combination of m, n. If j is even, then the corresponding polynomial is symmetric and for an odd j the polynomial is antisymmetric.

j	n	m	Z_j	Aberration Name
1	0	0	1	Piston
2	1	1	$2\rho\cos\theta$	x-tilt
3	1	1	$2\rho\sin\theta$	y-tilt
4	2	0	$\sqrt{3}(2\rho^2-1)$	Defocus
5	2	2	$\sqrt{6}\rho^2\sin 2\theta$	45 Primary astigmatism
6	2	2	$\sqrt{6}\rho^2\cos 2\theta$	0 Primary astigmatism
7	3	1	$\sqrt{8}(3\rho^3-2\rho)\sin\theta$	Primary y-coma
8	3	1	$\sqrt{8}(3\rho^3-2\rho)\cos\theta$	Primary x-coma
9	3	3	$\sqrt{8}\rho^3\sin 3\theta$	
10	3	3	$\sqrt{8}\rho^3\cos 3\theta$	
11	4	0	$\sqrt{5}(6\rho^4-6\rho^2+1)$	Primary spherical aberration
12	4	2	$\sqrt{10}(4\rho^4-3\rho^2)\cos 2\theta$	0 Secondary astigmatism
13	4	2	$\sqrt{10}(4\rho^4-3\rho^2)\sin 2\theta$	45 Secondary astigmatism

2.7 Phase retrieval

In order to determine the diffraction limited performance of a microscope and get information on the origin of aberrations, various methods are available [30] [31]. In this work a wavefront reconstruction algorithm based on non-linear optimization proposed by [23] is used to retrieve the wavefront in the exit pupil. The algorithm requires intensity measurements of defocused planes in the image space as shown in Figure 2.14.

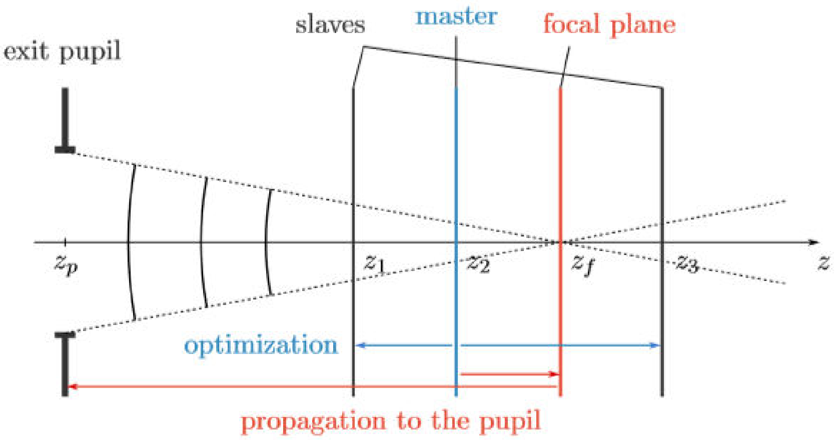

Figure 2.14: Illustration of the phase retrieval algorithm procedure. Optimization is done by propagating light fields between defocused planes with respect to a randomly chosen 'master plane' and minimizing their difference in phase. After the phase gradient has been minimized, the wavefront is propagated back to the exit pupil. Image taken from [24].

By measuring intensities I in a defocused planes, we chose one of them as the master plane, denoted with index j, then the relation

$$|F_j(x,y)| = \sqrt{I_j(x,y)} \tag{2.44}$$

can be used to find the complex field amplitude F with x and y being the pixel coordinates in the field. A numerical field G is then created by using one of the measured amplitudes and a randomly guessed phase $\theta_j(x,y)$

$$G_j(x,y) = |F_j(x,y)| e^{i\theta_j(x,y)}. \tag{2.45}$$

In each iteration cycle, this field is numerically propagated from the initial master plane to slave planes $k \neq j$ by angular spectrum propagation

$$G_{kj}(x,y) = \mathcal{F}^{-1}\left(\mathcal{F}(G_j(x,y)) T_{kj}(u,v)\right), \tag{2.46}$$

where $\mathcal{F}$ and $\mathcal{F}^{-1}$ are the discrete Fourier transform and the inverse one with the transfer function

$$T_{kj}(u,v) = e^{2\pi i \Delta z_{kj} \sqrt{1/\lambda^2 - (u^2+v^2)}}. \tag{2.47}$$

The transfer function in equation (2.47) considers the field propagated a distance Δz_{kj} from the jth to k^{kh} plane. In the next step, the fields are compared with the measured intensities in each of the slave planes by using a normalized sum of squared errors as an objective function

$$E_j = \frac{\sum_{k\neq j}\sum_{x,y}(|F_k(x,y)|-|G_{k,j}(x,y)|)^2}{\sum_{k\neq j}\sum_{x,y}|F_k(x,y)|^2}. \tag{2.48}$$

The minimum of equation 2.48 with respect to the phase $\phi_j(x,y)$ gives the best phase estimate in the master plane. To minimize E_j, the analytic expression for the gradient is introduced

$$\frac{\delta E_j}{\delta \phi_j(x,y)} = 2Im\frac{G_j(x,y)\sum_{k\neq j} G^{w*}_{jk}(x,y)}{\sum_{k\neq j}\sum_{x,y}|F_k(x,y)|^2}. \tag{2.49}$$

This is convenient because it is much faster to compute than other nonlinear optimization algorithms requiring second derivatives. $G^{w*}_{jk}(x,y)$ is defined as the inverse propagated field from kth to j^{kh} plane

$$G^{w}_{jk}(x,y) = |F_k(x,y)|e^{iarg(G_{kj}(x,y))} - G_{kj}(x,y). \tag{2.50}$$

For a given amount of measurement planes K, equation (2.49) features an effective way to compute the gradient for arrays of (pixel) size $N\cdot M$ using $2(K-1)$ propagations. Once the phase in the master plane is retrieved by the methods described above, the field is propagated to the focal plane by angular spectrum propagation, similar as in equation (2.46), and then inverse Fraunhofer diffraction is used to acquire the field in the exit pupil plane

$$G_p(p,q) = \mathcal{F}^{-1}\left(G_f(x,y)e^{-\frac{i\pi}{\lambda\Delta z_{fp}}(x^2+y^2)}\right). \tag{2.51}$$

Coordinates p,q represent exit pupil coordinates and Δz_{fp} is the distance from exit pupil to focal plane. Eventually, the complex phase of $G_p(p,q)$ can be related to the wavefront error by

$$W(p,q) = \frac{\lambda}{2\pi}argG_p(p,q). \tag{2.52}$$

2.8 Image quality

There are several ways to evaluate image quality by utilizing ray tracing. Some of the standard tools that most optical design software products feautre are about to be discussed.

2.8.1 Spot diagram

The standard spot size diagram displays the cross section of the ray distribution according to ray tracying in the plane of interest. An example is shown in Figure 2.15.

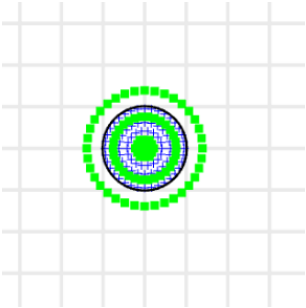

Figure 2.15: A spot diagram showing the cross section of rays in a plane in image space.

The quantity that can be retrieved from it is the root mean square radius $r_{rms} = \sqrt{\frac{\sum^{n} |r_i - r_c|^2}{n}}$ for n rays and the center ray r_c. The spot diagram is particularly helpful in the early design stages to get a good estimate on the resolution and aberrations present in the system [32].

2.8.2 Strehl ratio

The Strehl ratio S is a quantity that compares the irradiance of the center peak in the aberration free diffraction pattern with the aberrated one. This can be stated as

$$S = \frac{I_a(0)}{I_u(0)} = \frac{h_a(0)}{h_u(0)}, \tag{2.53}$$

which is the ratio of the center peak intensities or the ratio of the point spread functions with the indices a and u denoting the aberrated and unaberrated system. However, a more applicable expression for the Strehl ratio is

$$S \approx e^{-(\frac{2\pi}{\lambda} W_{rms})^2} \tag{2.54}$$

with the wavefront error W_{rms}. This, however, only holds true if the aberrations are sufficiently small. It is generally defined that the wavefront error has to satisfy the condition $W_{rms} \leq \frac{\lambda}{14}$, such that equation (2.54) is a good approximation, which equals a Strehl ratio of 0,8 [28]. Furthermore, a system is considered diffraction limited if this approximation holds true. With this definition, phase retrieval can be used to extract the wavefront in the exit pupil and with Zernike polynomial fitting on the wavefront map W_{rms} is calculated to eventually get the Strehl ratio.

2.8.3 Modulation transfer function

Aside from resolution, another important property to describe the visual quality of an image is contrast, which essentially compares the singal regions to the surrounding background. Contrast m has a straightforward interpretation of

$$m = \frac{I_{max} - I_{min}}{I_{max} + I_{min}}. \tag{2.55}$$

However, imaging systems impose a resolution dependet limit on the transfer of contrast from object to image plane. The modulation transfer function (MTF) $|H(f_x, f_y)|$ describes the loss of contrast of an optical system, given by

$$|H(f_x, f_y)| = \left| \frac{\iint_{-\infty}^{\infty} |h(u,v)|^2 e^{-i2\pi(f_x u + f_y v)} du dv}{\iint_{-\infty}^{\infty} |h(u,v)|^2 du dv} \right|. \tag{2.56}$$

As we can see from equation (2.56), the MTF is the Fourier spectrum of the PSF $h(u, v)$, normalized by background. MTF plots are a commonly used and powerful tool to quantify imaging systems because they show the loss of contrast depending on spatial frequency, which holds more information about the system than single numbers like the strehl ratio or the rms spot size. The spatial frequency in an MTF plot corresponds to resolution and has a cutoff frequency of $f_c = \frac{2NA}{\lambda}$. Beyond the cutoff frequency, objects can no longer be resolved. The effect of aberrations in an imaging system lower the transfer of contrast, while the cutoff frequency is unaffected as shown in Figure 2.16.

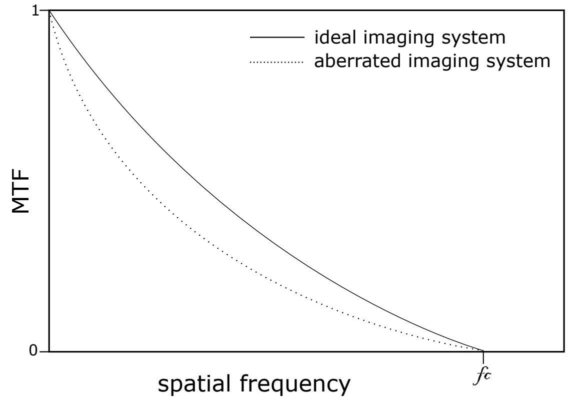

Figure 2.16: Illustrated modulation transfer function. A real imaging system will always have a lower modulation due to arbitrary aberrations. It will however, have the same cutoff frequency f_c as the ideal imaging system according to diffraction theory.

3 Designing and modelling of the objective

Nowadays, there are various ray tracing software products available to assist in designing and analysing optical systems. However, these tools typically do not instruct the user in developing the actual design. Hence, a good knowledge of the basic concepts of microscopy is useful to develop a design which delivers a satisfying performance for given conditions. The software is basically assisting by varying parameters like lens thickness, radii and the distances between elements until the quantity of interest reaches a satisfying value while any boundary constraints are upheld. This quantity can be for example the focal length of the system, the radial spot size of converging beams or the wavefront error. In this work the software OpticStudio is used for this task and the quantity of interest is the wavefront error.

3.1 Design considerations

There are several design challenges that come along when imaging ultracold quantum gas mixtures. First of all, the sample is located in an ultra-high vacuum environment and thus surrounded by a glass cell with a thickness of typically a few millimetres which introduces significant spherical and chromatic aberrations. The position of the gas cloud inside the vacuum chamber is not precisely known, therefore the objective should either feature a movable focusing lens to adjust the focus depth or be entirely movable to control the working distance. The imagining wavelength for the lithium-potassium mixture are 671 nm and 766 nm, and are supposed to be imaged on two different cameras so the beam will pass a beamsplitter at some point before the image is formed. To remove additional spherical aberrations induced by converging light rays passing through a beamsplitter, the concept of infinite conjugate imaging can be applied. In such systems, the objective itself does not form an image but a collimated beam which forms the image at infinity. Hence, one can put a beamsplitter in the collimated beam path to separate the imaging beams without having to worry about additional aberrations. After the beamsplitters, a lens for image forming can be placed in each path. Once a lens system is optimized, it should feature diffraction limited performance (Strehl ratio >0.8) for both wavelengths over an appropriate field of view in the order of a few tens of micrometers. In addition, achieving achromatic performance is seen as an optional goal, which would allow both wavelength to be imaged on the same camera without having to adjust the focus.

3.1.1 Imaging through polarizing optics

A special case to consider in this experiment is the implementation of an optical element that substitutes all the optics required for the one of the magneto-optical trap (MOT) beams. It is essentially made of a $\lambda/4$ plate followed by a wire grid polarizer, oriented 45° to the $\lambda/4$ plate. This element reflects light polarized parallel to the wire grid while light perpendicular to it passes through. It is placed on top of the glass cell in the path of the bottom MOT beam and will reflect the beam, such that from the atom's point of view as a MOT beam coming from the top. The imaging beams are travelling the same path as the bottom MOT beam but those are going to pass the grid due to their polarization. This trick is used to remove the optics required for the top MOT beam and provides sufficient free space to place the objective close on top of the cell, which increases the numerical aperture of the system substantially. While the exact material composition of this polarizer is unknown, its refraction index is known and can thus be modelled in OpticStudio as another glass plate on top of the glass cell. A simplified picture of the apparatus is shown in Figure 3.1

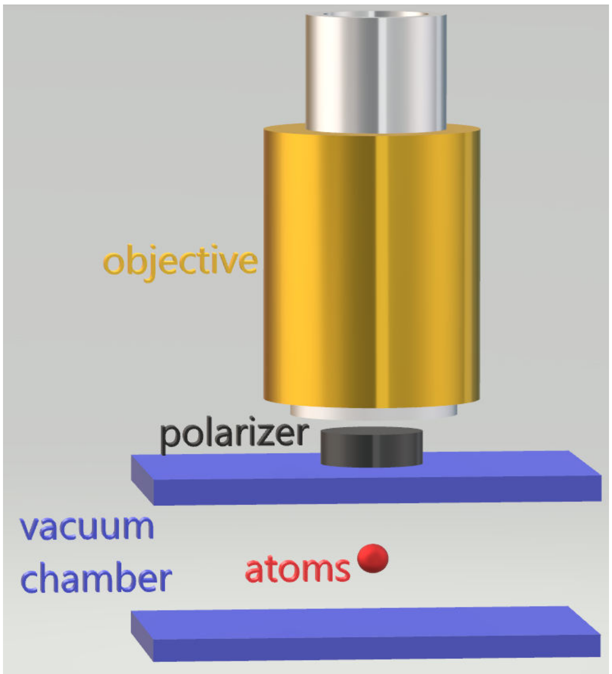

Figure 3.1: Schematic experimental setup with a microscope objective, a polarizer element and the vacuum chamber housing the atoms.

3.1.2 Lens shapes

The behaviour of aberrations depending on the lens shape is reviewed in Figure 3.2.

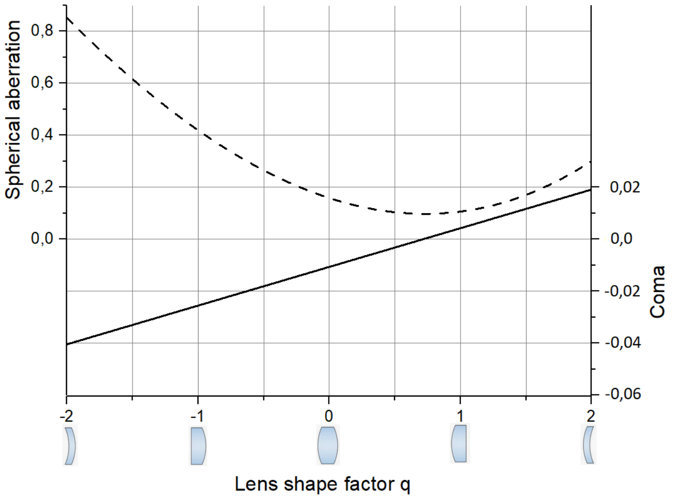

Figure 3.2: Axial difference of the focal length in cm as a function of the lens shape factor q, with the correponding lens drawn below the x-axis for $q = -2, -1, 0, 1, 2$. The two curves, representing spherical aberrations (dashed line) and coma (solid line), show the magnitude of axial dispalcement of the focal point. The data was taken by raytracing with lenses that feature the same index of refraction and a focal length of 10 cm [33]. The shape factor $q = \frac{r_2+r_1}{r_2-r_1}$ is a common quantity to characterize lenses, where $r_{1,2}$ are the lens radii.

The plot in Figure 3.2 shows a few interesting properties, as for example the focal point displacement by coma can be reduced to zero for $q = 0.8$ while the one for spherical aberrations is always nonzero for typical lenses. One would think, that picking only lenses near the spherical aberrations graph's minimum would provide the best result, which is, in fact, true for many applications. However, it has already been mentioned that imaging through a glass window induces spherical aberrations before the light cone hits the objective. In some cases, it can be useful to pick lenses with higher spherical aberration if they have the opposite sign of those already present in the system. Finding the right shape will be the task of the raytracing software. Commercial retail lenses are rarely available with the ideal curvatures, but we can use multiple commercial lenses to achieve a satisfying performance without requiring custom lenses.

3.1.3 Magnification

The magnification will be set by the image forming lens after the infinite conjugate plane, however to avoid undersampling on the CCD chip the magnification should satisfy $|M| > \frac{4d_{px} \cdot NA_o}{\lambda}$. Regardless of the final design, the detector pixel size of our CCD chip is known to be 6.8 μm and the smaller imaging wavelength is 671 nm. Microscopes in quantum gas experiments, that are not quantum gas microscopes, usually have a numerical aperture of 0.5-0.6. In that case the criteria would require the magnification $|M| > 20.3$ or $|M| > 24.3$ in the latter case. It is a lesser problem to worry about, since there is some room to adjust the magnification with the imaging lens in the infinite conjugate plane.

3.2 Considered design

After various different design approaches were made, a design which satisfies all conditions was generated by Emil Kirilov, senior scientist of the group. The lens assembly is shown in Figure 3.3 and a table with lens specification in table 3.4.

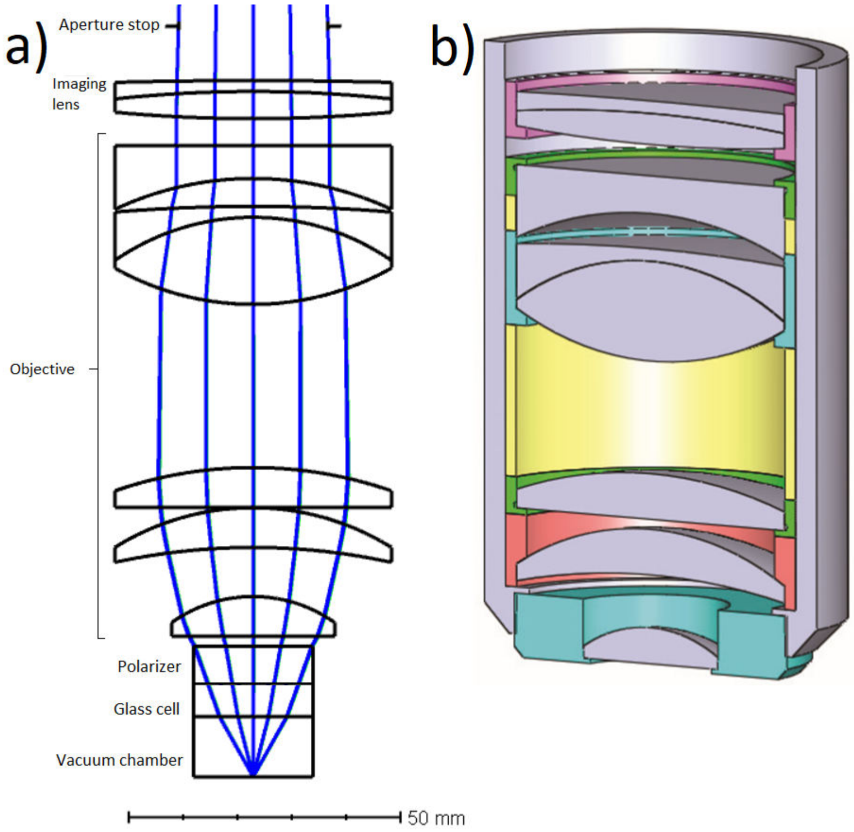

Figure 3.3: a) A 2D lens profile of the setup. The blue lines indicate the light's path through the system. The two outmost beams are known as the marginal rays, which define the numerical aperture. The aperture stop at the top is an iris diaphragm, which sets the numerical aperture in the system. b) Cross section of the objective tube with the lenses in place. The lenses are held in place by spacer rings where the lens bed is following the lens curvatures. This is supposed to ensure a more precise lens placement than with optical glueing or using standard retaining rings. The front lens holder at the very bottom is movable along the vertical axis to move the focus.

Table 3.4: Table of lens parameters in the design. All values are in mm.

	Surf:Type	Comment	Radius	Thickness	Material	Coating	Clear Semi-Dia
0	OBJECT Standard ▾	Object plane	Infinity	985,000			0,863
1	STOP Standard ▾	Iris diaphragm	Infinity	10,000			13,302
2	(aper) Standard ▾	AC508-1000-B	-3440,...	2,800	SF10	THORBSLAH64	25,400
3	(aper) Standard ▾		398,100	4,200	N-BAF10		25,400
4	(aper) Standard ▾		-494,3...	5,000		THORBSLAH64	25,400
5	(aper) Standard ▾	Swarovski lens	Infinity	6,000	N-SF66	THORB	25,400
6	(aper) Standard ▾		59,690	5,210			25,400
7	(aper) Standard ▾	AC508-080-B	312,600	2,000	N-SF6HT	THORBSLAH64	25,400
8	(aper) Standard ▾		44,600	16,000	N-BAF10		25,400
9	(aper) Standard ▾		-51,800	30,012		THORBSLAH64	25,400
10	(aper) Standard ▾	LA1417	77,300	7,300	N-BK7	THORB	25,400
11	(aper) Standard ▾		Infinity	0,109		THORB	25,400
12	(aper) Standard ▾	LE1418	47,900	7,300	N-BK7		25,400
13	(aper) Standard ▾		119,300	9,069			25,400
14	(aper) Standard ▾	LA1102	25,800	7,300	N-BK7	THORB	15,000
15	(aper) Standard ▾		Infinity	1,814		THORB	15,000
16	(aper) Standard ▾		Infinity	13,000	SILICA		12,700
17	(aper) Standard ▾		Infinity	11,000	VACUUM		12,700
18	IMAGE Standard ▾	Image plane	Infinity	-			12,700

3.3 Estimated performance

The ray tracing optimization was set to minimize the wavefront error as suggested in [24]. This comes at the cost of a lower peak Strehl ratio on-axis but a an overall higher Strehl ratio for off-axis points. Figure 3.5 shows the Strehl ratio as a function of off-axis distance.

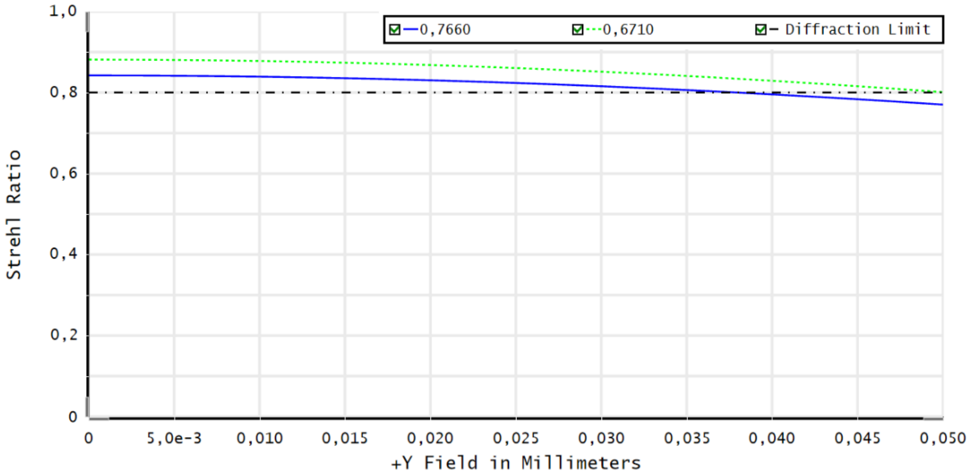

Figure 3.5: Strehl ratio as a function of off-axis distance. The solid line corresponds to 766 nm light and the dashed line to 671 nm. The dash-dotted line at 0.8 marks the diffraction limit.

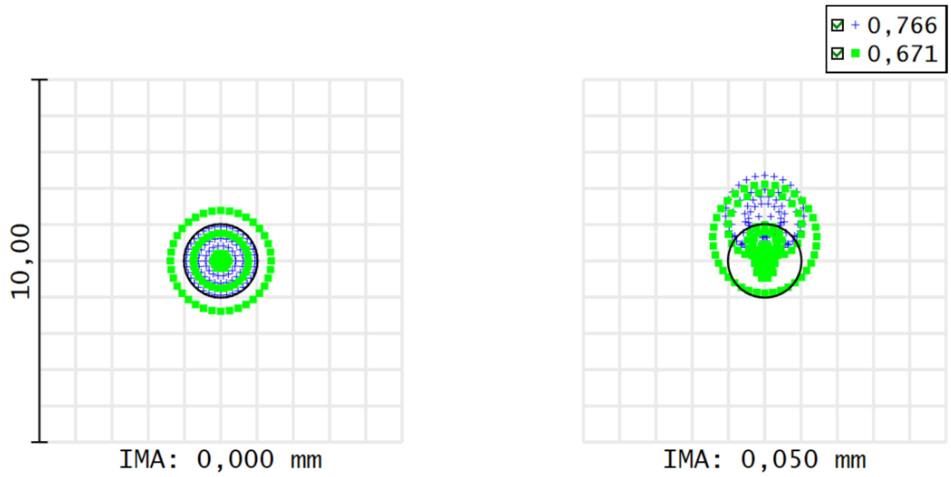

Figure 3.6: Spot diagrams for both wavelength. The left diagram shows the on axis spot and the right one 50 microns off the focus, each for an aperture stop diameter of 24 mm. The entire field shown measures 10x10 μm.

According to the ray tracing simulation the field of view should be roughly 80 μm and 100 μm with peak Strehl ratio values of 0.83 and 0.87 for 766 nm and 671 nm respectively. The spot diagrams give an estimate of the broadened instensity distribution due to wavefront errors. If there were no aberrations in the systems, all rays would converge to the image plane strictly by diffraction theory. From the spot diagrams in Figure 3.6 the on-axis Airy disk radius is indicated as solid line and yields $r_0^{766} = 1.093$ μm and $r_0^{671} = 0.957$ μm for the respective wavelength. The achromatic performance is shown in Figure 3.7.

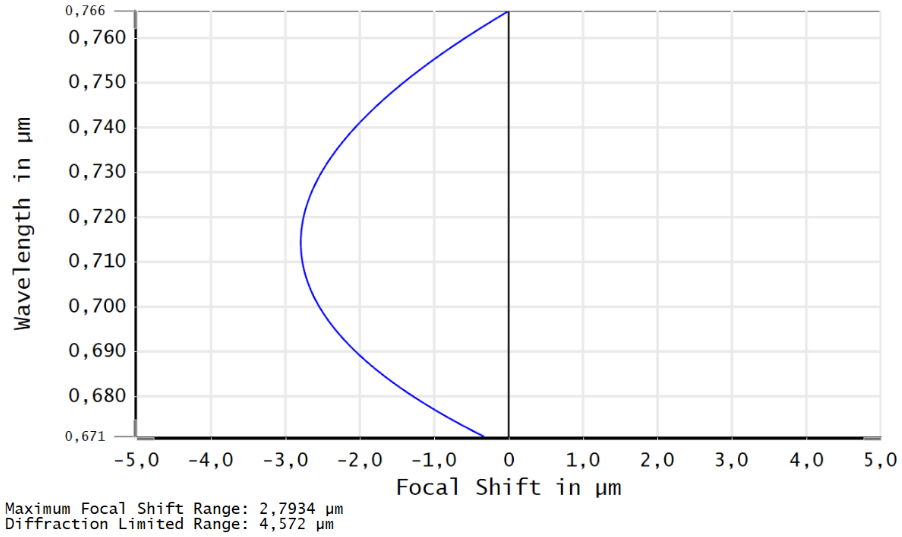

Figure 3.7: Wavelength as a function of focal shift between 671 nm and 766 nm. The intersection of the solid curved line with the x-axis marks the focal shift and yields $\Delta = 0.424$ μm.

The results show, that the chromatic focal shift $\Delta = 0.424\ \mu$m is below the diffraction limited range of $4,57\ \mu$m. The diagrams for the optical path difference in figure 3.8 and the MTF in figure 3.9 are included for completeness, however the MTF is not a subject to be investigated in the experimental part. The topic of wavefront error in association with optical path difference was discussed in chapter 2.

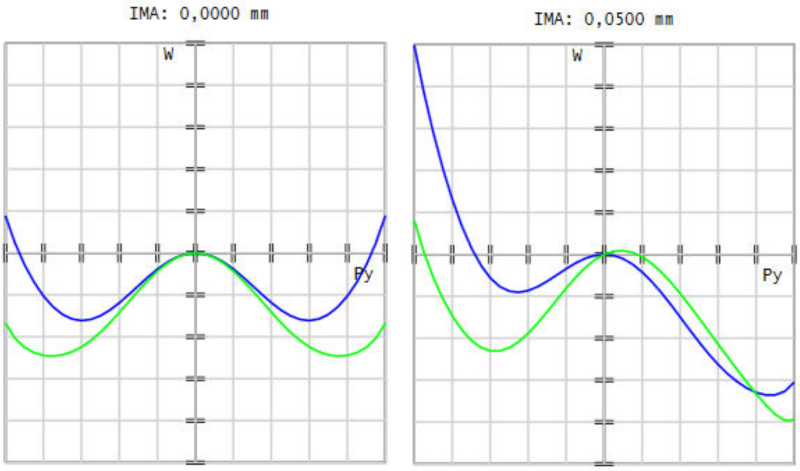

Figure 3.8: Optical path difference as a function of pupil coordinate on-axis (left) and 50 microns off-axis (right).

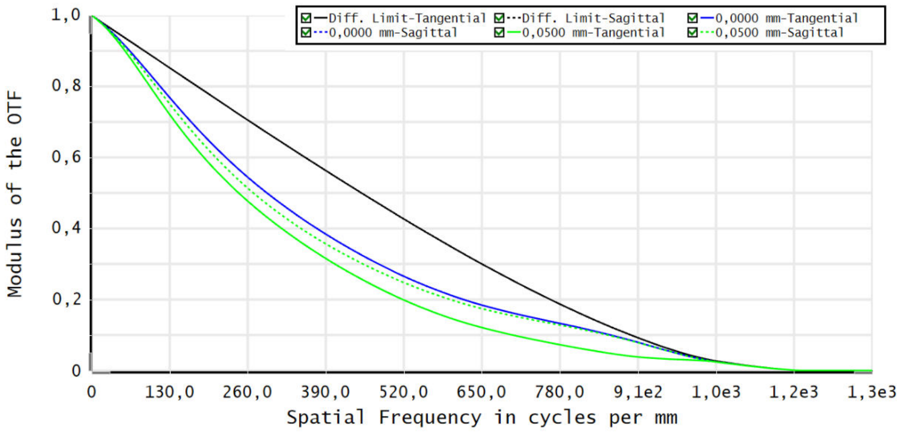

Figure 3.9: The modulation transfer function for 766 nm indicating the performance of resolution and contrast as spatial frequency increases. The blue lines show on-axis performance and the green ones show 50 micron off-axis performance, whereas the solid lines correspond to the tangential plane and the dashed lines to the sagittal plane. The solid black line is the ideal aberration free MTF.

4 Experimental characterization of the objective

This chapter focuses on the experimental work carried out to test the microscope's performance. A setup is assembled to carry out two similar but independent measurement methods, and the results are presented below. The first measurement method involves the examination of a 500 nm pinhole where monochromatic light is sent through. Once the objective-pinhole system is properly aligned, the light passing through the pinhole proceeds through the objective and gets focused onto a CCD chip. As the pinhole features a circular opening with a radius below the microscopes resolution limit, it is expected to see an Airy pattern on the CCD and the disks zero order radius corresponds to the resolution limit. In general, if the aperture of the light source is smaller than the resolution limit, there is no significant difference to an ideal point source.

While magnification and resolution are straight forward measurements which do not require much computational effort, the calculation of the Strehl ratio is based on the algorithm explained in section 2.7. With the Strehl ratio known, the field of view can be quantified as well. At last the focal shift between the two wavelengths of interest is measured. The second measurement method uses the same setup, but the pinhole is replaced by a SNOM fiber with a 100 nm tip. The idea behind the SNOM fiber measurement is primarily to verify the resolution limit provided by the pinhole. Beyond that, SNOM fibers are very useful in high resolution microscopy because of the small tip diameter and wide angle of light emission. For optical microscopes with high numerical aperture, and by using blue light, the resolution limit can easily be pushed below 500 nm where commercial pinholes are not known to exist. In such cases, SNOM fiber probes can provide a light source with an aperture of 70 nm.

4.1 Experimental setup

To test the microscope's performance, a test setup as shown in 4.1 is assembled. The criteria for this setup are that both, camera and pinhole, are movable along the optical axis for defocus (z-axis) and the pinhole needs to be movable orthogonally to the optical axis (x- and y-axis).

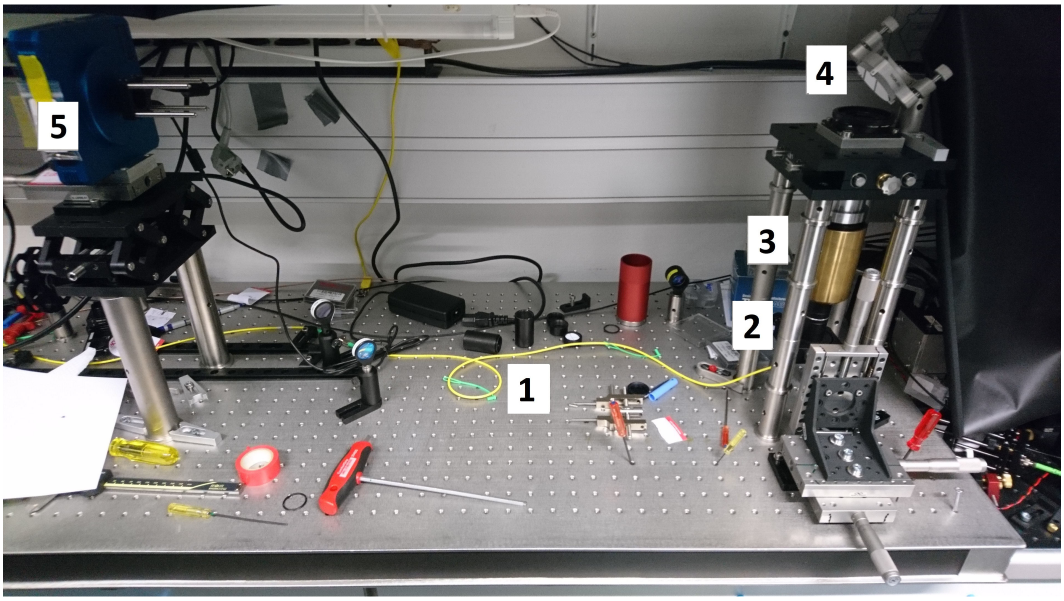

Figure 4.1: Experimental setup for characterizing the microscope. Via an optical fiber cable (1) either 766 nm or 671 nm light is guided to a tube system where the pinhole is located (2). The microscope sits above it in the golden tube (3) and atop a mirror (4). A camera is put along the optical path at (5).

A MOGLabs cateye diode laser is used as a source for the 766 nm and a M squared TiSa laser for the 671 nm. The light is guided by a fiber into the tube apparatus, shown in Figure 4.2, where the pinhole is located. The light gets diffracted at the pinhole and propagates further through a glass plate and the MOT reflecting piece. The glass plate shall imitate the top glass cell wall of the vacuum apparatus as discussed in chapter 3. The light leaving the tube will further pass through the microscope and atop of it through an iris diaphragm which serves as an aperture stop with a maximum diameter of 25 mm. Then, a mirror is used, for convenience, to avoid having to mount the CCD camera one meter in the air above the microscope. Eventually, the light is collected by an Apogee Alta F32 CCD camera which is placed on two translation stages to adjust height and depth along the optical path. The distance of the Camera is initially set to be roughly 85 cm away from the mirror, and the distance from the mirror to the last achromatic lens of the microscope is about 15 cm. This ensures that the camera is close to the achromat's $f = 1$ m focal length. The microscope itself features a movable front lens and a detachable lens holder after the infinite conjugate plane, as shown in Figure 4.2.

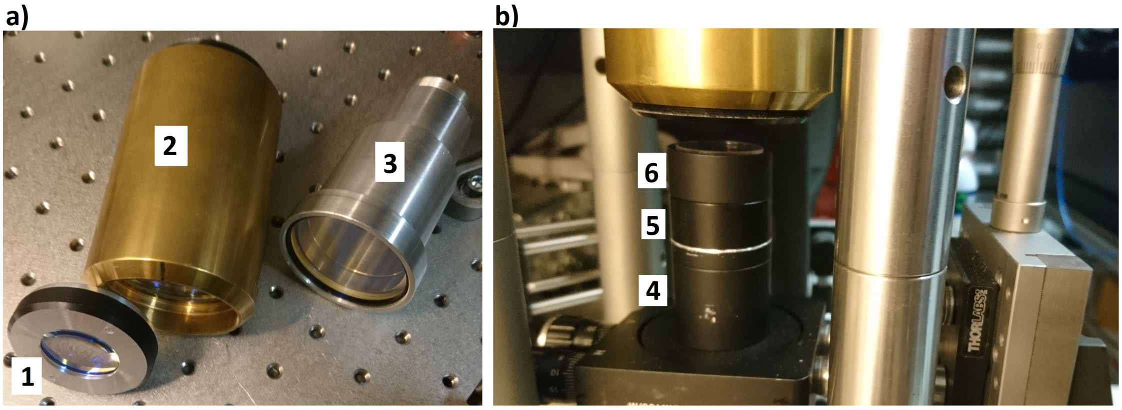

Figure 4.2: a) Disassembled microscope with 1) the microscope front lens, 2) the microscope tube, housing all other lenses until the infinite conjugate plane, and 3) the back achromatic lens defining the focal length. The objective's design allows to exchange the last lens in the microscope, which features easier switching of the focal length. The working distance can be changed by rotating the front lens for about 5 mm. b) Close up image of the tube, housing the fiber connection (4), providing light to illuminate the pinhole from below (5) and the glass plate and MOT reflecting piece atop of it (6). This tube is mounted on a tiltable plate on a XYZ translation stage. The microscope is embedded in the golden tube above, which is mounted independently of the translation stage.

The objective's design allows to exchange the last lens in the microscope, which features easier switching of the focal length. The working distance can be changed by rotating the front lens for about 5 mm.

4.2 Pinhole measurements

Before any measurements can be done, the pinhole-objective-camera setup has to be aligned. This can be done by having the camera in the correct focus position of the last achromatic lens and then using the XYZ translation stage to get the pinhole in the working distance and the field of view. Once the Airy spot can be observed on the camera, any obvious tilts and comas can be corrected by defocusing the pinhole a bit to see more rings of the Airy disk. By seeing more rings, it is easier to visually identify any bias in the intensity distribution which can then be corrected by using XY translation axis and the tilt plate. Once the system is well corrected, the measurement process begins. The camera is operated with the open source microscopy software Micromanager and for early image processing ImageJ is used. ImageJ has some great features built in that are very useful in the early testing stages. An example of a defocused pinhole image and its profile plot is shown in Figure 4.3.

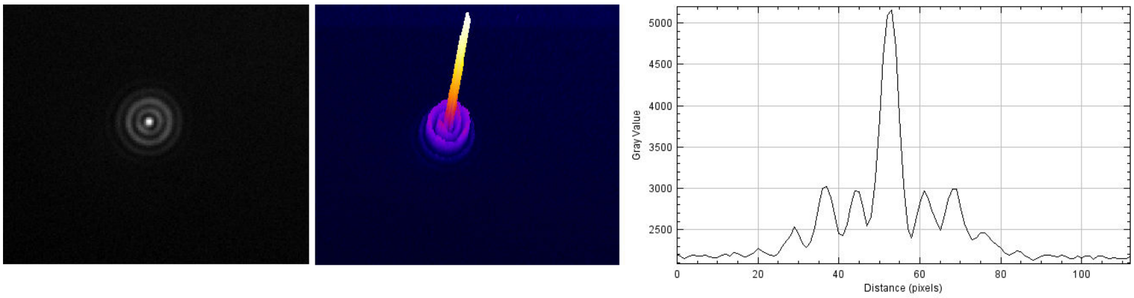

Figure 4.3: Left: raw intensity image of the pinhole in a defocused plane. Center: 3D intensity plot of the same image. Right: intensity profile of a horizontal slice through the center of the airy disk. The image was taken for an exposure time of 50 ms.

The quality of these images can be improved by using the subtract background process, which features two utilities. It enhances the image quality by replacing each pixel value with the average of the surrounding 3x3 pixels to reduce noise and then subtracts background. A method known as the rolling ball algorithm [34] is used to subtract the background in images, which is in particular useful because it corrects non constant background well. An example is given in Figure 4.4.

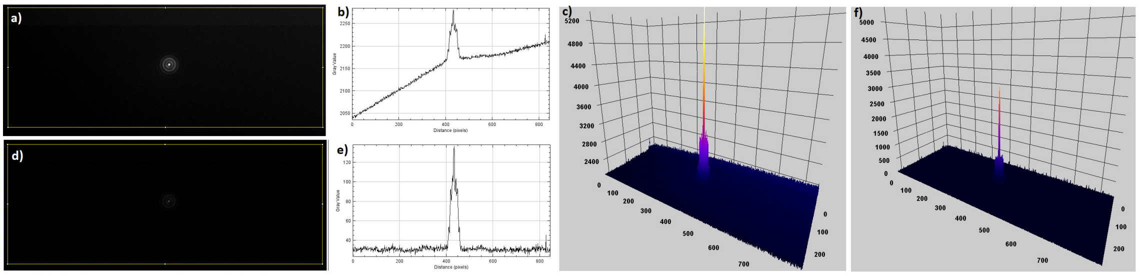

Figure 4.4: Showing the effect of the background subtraction tool in ImageJ. a) Raw image of the same spot as in Figure 4.3. b) Intensity profile inside the yellow rectangle in a), the x-axis shows the horizontal distance and the y-axis is the vertically averaged pixel intensity. c) 3D profile of the raw image. d) Raw image after performing background subtraction and smoothing. e) Averaged intensity profile of d), now showing a reduced and rather constant background. f) 3D profile of d).

Using the background subtraction in ImageJ makes further processing easier. The smoothing supresses artifacts caused by defect pixels and smoothens the peak intensity in the airy disk center, which allows a more precise determination of the center. The rolling ball algorythm creates the background by scanning the backside of the surface of the intensity map with a paraboloid of some radius of curvature and then subtracts that background from the intensity map. Care has to be taken as the radius of curvature is entered by the user and may not be chosen too small, because it would treat more of the signal region as background as well, the smaller the radius get. Hence, a radius much larger than the signal is preferred and was chosen to be 100 pixel. Conventional background subtraction by taking a the average intensity of a ring around the signal region and subtracting it will eventually remove the remaining background properly, but both methods combined seem to be the best solution. Such irregularities in background intensity as showcased in Figure 4.4 were avoided in actual measurements, but the method has proven to be effective even in extreme cases.

4.2.1 Magnification

In order to measure the objectives magnification, the pinhole is displaced stepwise along the xy plane and for each step the position of the Airy disk on the CCD is recorded. Since the pixel size of the camera is known to be 6,8 μm, the relation

$$d_{img} = M \cdot d_{obj} \tag{4.1}$$

can be used to determine the magnification M from the displacements in object space d_{obj} and image space d_{img}. This measurement is done for the x and y axis of the translation stage independently to possibly identify systematic errors. The results with 766 nm light are shown in Figure 4.5.

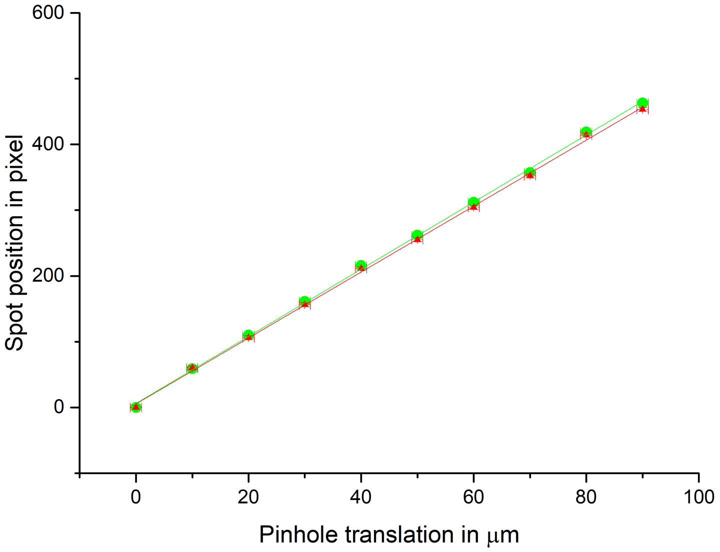

Figure 4.5: Measurement for the magnification. The pinhole is moved in 10 μm steps and the spot position on the CCD chip gets mapped. The two different colours each correspond to one axis. Two linear fits with x error of the form $y = kx + d$ are fitted to get the magnification. From the fits the parameters k_x=5,01(5) $\frac{\text{pixel}}{\mu\text{m}}$ and k_y=5,12(5) $\frac{\text{pixel}}{\mu\text{m}}$ are obtained. Parameter d is fixed at zero.

The magnification can be calculated with the slopes retrieved in Figure 4.5 to

$$M = 34,4(4), \tag{4.2}$$

where M corresponds to the arithmetic mean of M_x and M_y. As both values are within 2.5σ of each other, their difference can be seen as statistical fluctuation. Furthermore, this value is also used for the 671 nm measurements.

4.2.2 Resolution

To verify the resolution experimentally, several shots of the pinhole are made in the focal plane. Then, Gaussian fits are applied to determine the full width at half maximum (FWHM), corresponding to the experimental resolution. Figure 4.6 shows the results of 10 shots for each wavelength with an aperture stop diameter of 17 mm and the average resolution measured and corrected by the magnification. The stop diameter at 17 mm showed the best resolution and is used for all subsequent measurements in this section.

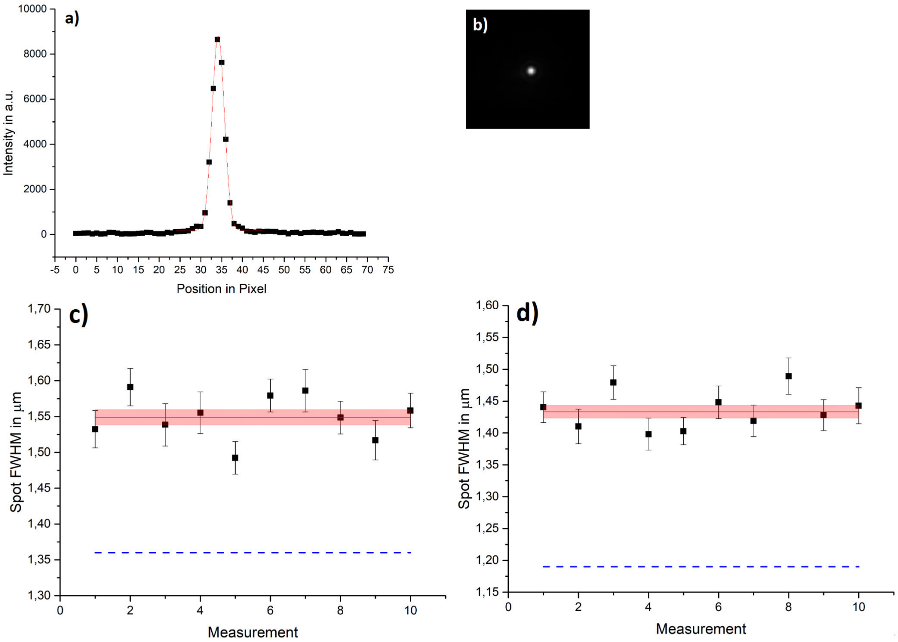

Figure 4.6: a) Gaussian fit to extract the FWHM of a point source (b) after background substraction. c) Measurement for 766 nm. A constant fit $y = d$ is fitted through 10 measurement points to gain the average spot radius at FWHM=1.55(1) μm with χ^2_ν=1,5. The red shaded region shows the 1σ confidence interval. The dashed line at 1,36 μm is the Rayleigh limit. d) Measurement for 671 nm. The constant fit $y = d$ provides the average value for the spot radius at FWHM=1.43(1) μm and χ^2_ν=1,4. The reference dashed fit at 1,19 μm represents the theoretical resolution limit.

Following the results from Figure 4.6, the measured resolution for each wavelength is

$$\mathrm{FWHM}^{766} = 1,55(1)\ \mu\mathrm{m}$$

$$\mathrm{FWHM}^{671} = 1,43(1)\ \mu\mathrm{m}.$$

The uncertainties in each measurement point in c) and d) in figure 4.6 are the fit errors from the FWHM parameter in the Gaussian fit. The discrepancy to the theoretical resolution limit, which is certainly larger than 5σ, may be caused by aberrations.

4.2.3 Strehl ratio

With the magnification and resolution known, the next quantity of interest is the Strehl ratio, as it is further required to quantify the field of view, as well as the focal shift. To retrieve it, the algorithm which was described in section 2.7 is applied. As the simulation estimates the objectives wavefront error to be smaller than $\lambda/14$, the relation

$$S \approx e^{-(2\pi W_{rms})^2} \tag{4.3}$$

can be used to approximate the Strehl ratio. A Python code to execute wavefront reconstruction by Zernike polynomial fitting was written by Miroslaw Marszalek and is used in this work [24]. A series of intensity measurements of the Airy disk around the focus is required to do a wavefront reconstruction, therefore a total of 100 images for both wavelengths are taken ±20 mm of the focus along the imaging axis. Some image processing is required prior to using them for wavefront reconstruction.

All defocused images have to be normalized by the total power to obtain correct relative intensities between defocused images. In the first step, the total power of each image gets estimated by summing up all the pixel values around the center peak. Then the background is estimated by taking the average pixel value of a circular region far from the signal region. By fitting a $y = A \cdot sinc^2(a(x-x0))$ function through power normalized peak intensities against defocus, the correct relative position from the image to the focus spot is extracted. Images are then cropped, get background subtracted and normalized by power and are further used for phase retrieval. A total of 20 optimization runs with 500 iterations with 2 images each are performed. The extracted Zernike polynomials are shown in figure 4.7 and figure 4.8. The results provide the first 40 Zernike coefficients which are used to calculate the W_{rms} and Strehl ratio values S for both wavelengths, with piston and tilt not included

$$W^{671}_{rms} = 0,0531(2), S^{671} = 0,894(3)$$

$$W^{766}_{rms} = 0,0574(3), S^{766} = 0,878(5).$$

The predicted values from the simulation S^{671}_{theory}=0.86 and S^{766}_{theory}=0.83 are statistically significantly lower than the measured results. This seems to be reasonable, since a bigger aperture stop diameter of 24,8 mm was used in the simulation, which gives rise to spehrical aberrations, reducing the Strehl ratio.

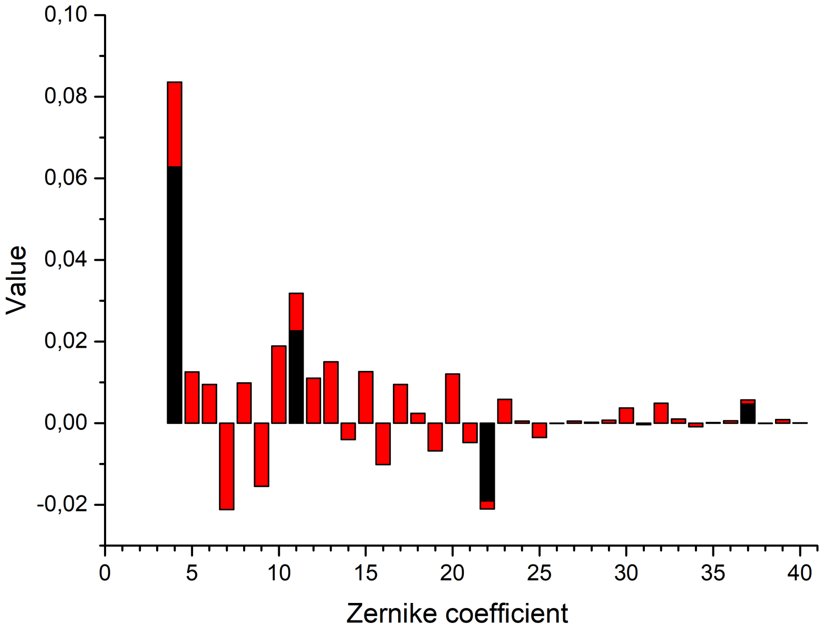

Figure 4.7: Zernike polynomials extracted from phase retrieval for 766 nm. The values in black represent the predicted ones by Zemax and the red bars are the experimental results. Error bars have been obtained by averaging multiple optimization runs, they do not appear due to their small size though.

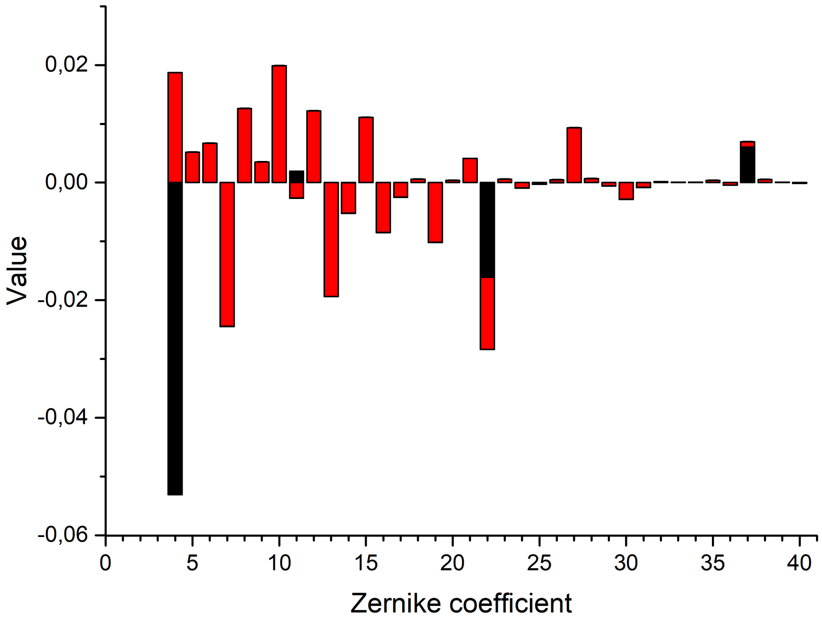

Figure 4.8: Phase retrieval results for 671 nm. The black bars show the predicted values and the red bars are the retrieved ones.

4.2.4 Field of view

In real experiments, the region of interest likely exceeds the diameter of a diffraction limited spot. Therefore, it is crucial to know how large the area around the optical axis is where the microscope still provides a Strehl ratio greater than 0,8. This diffraction limited area is known as the field of view (FOV).

Displacing the pinhole orthogonal to the optical axis causes an peak intensity loss which is directly connected to the loss of Strehl ratio. Comparing the peak intensities of power normalized images off-axis with the known on-axis Strehl ratio value from phase retrieval, allows to determine the field of view. The results for both wavelengths are presented in Figure 4.9.

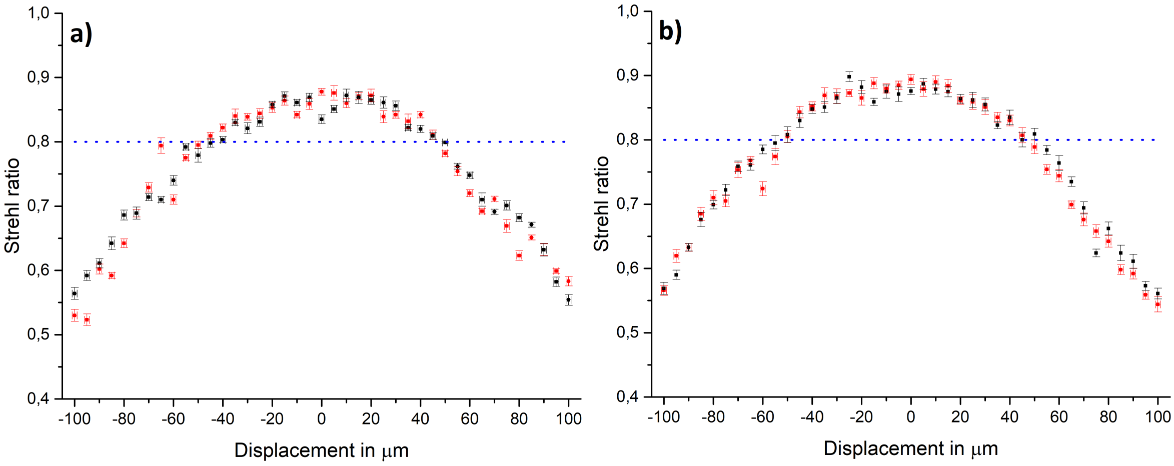

Figure 4.9: Measurements for a) 766 nm and b) 671 nm. The two colours indicate the x- and y-axis orthogonal to each other and to the optical axis. Each data point is an average of 3 points measured in the same position. The dashed line is the diffraction limit or Strehl ratio=0,8.

From the data presented in 4.9, the field of view is estimated to be

$$\mathrm{FOV}^{766} \approx 90\ \mu\mathrm{m},$$

$$\mathrm{FOV}^{671} \approx 110\ \mu\mathrm{m}.$$

The fov in the simulation with the same aperture stop of 17 mm should roughly be twice as large, which is most likely caused by larger spherical aberration, coma and astigmatism than the simulation predicts.

4.2.5 Chromatic focal shift

As the refractive index is a function of wavelength due to dispersion, the microscope uses achromatic lenses to reduce the magnitude of the chromatic focal shift between both wavelengths. To quantify this shift, the peak intensity loss is being measured for both wavelengths when moving the camera out of the focus along the optical axis while keeping the pinhole in the same position. It follows the same principle as in section 4.2.4, by comparing normalized peak intensities. The results are shown in Figure 4.10.

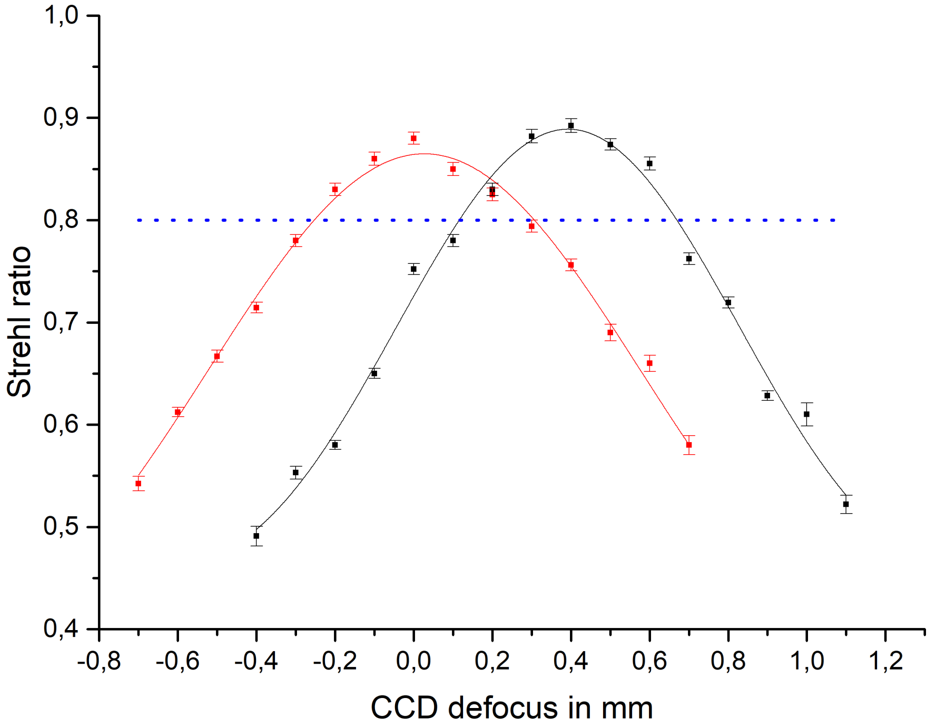

Figure 4.10: Measurement for the focal shift between both wavelengths. Left (red) data are for 766 nm and right (black) for 671 nm. Two fits of the form $y = A \cdot sinc^2(b(x - x_0)) + y0$ are used to extract peak position at x_0. The parameters x_0^{766}=0,391(7) mm and x_0^{671}=0,024(5) mm are obtained. The dashed line indicates the diffraction limit.

With the data from Figure 4.10, the focal shift is deduced to

$$\Delta x_0 = 0,37(1) \text{ mm}. \tag{4.4}$$

Another information that can be extracted is the field where both wavelengths are diffraction limited. The narrow overlap area is 0,2 mm in width.

4.3 SNOM fiber measurement

In this section, experimental work carried out with a 100(30) nm SNOM fiber tip at 766 nm is presented. The measurements presented are supposed to verify the results independently of the pinhole. Especially with a resolution being far off the estimate, the pinhole itself would come into question as an error source as well.

4.3.1 Experimental adaptation to probe a SNOM tip

There is a little experimental alteration required to operate the SNOM fiber with the current setup. The items used to utilize the SNOM are shown in Figure 4.11.

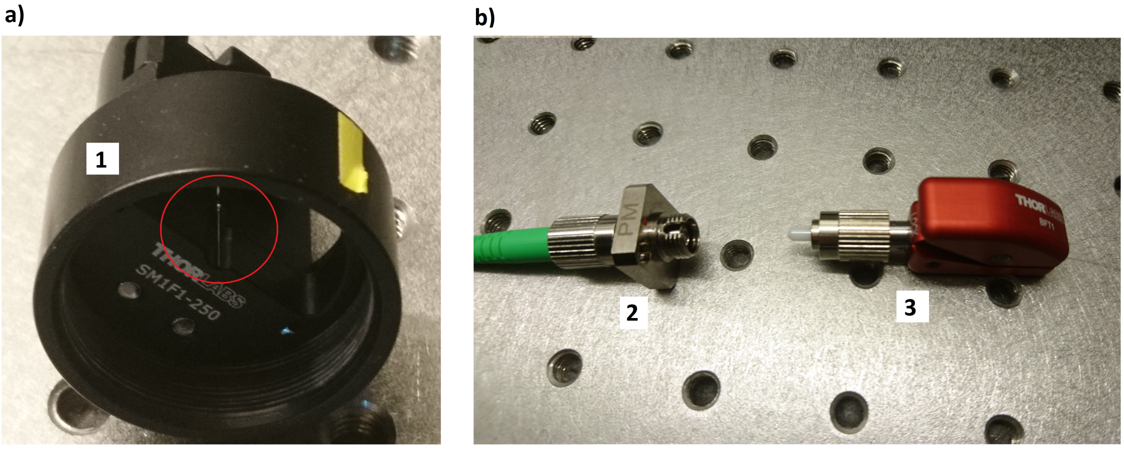

Figure 4.11: Tools used to operate the SNOM fiber probe. a) (1) A SM1F1-250 fiber clamp holding the tip of the SNOM fiber (encircled in red). b) The other end of the fiber is guided through a single mode/polarization-maintaining fiber connector (3) which can be connected to one side of a fiber connector adapter (2). The fiber connected to the opposite side of the adapter provides the light source.

The fiber clamp inside the tube in Figure 4.11 is used to maintain the SNOM fiber tip, centered within the tube for easier probing under the microscope. This tube replaces part 4 and 5 in caption 4.1 and part 6 is screwed on top of the clamp tube. Thus the light emitted from the SNOM tip propagates along the same path as the one from the pinhole. Prior to the measurements, the spot is once again corrected to obvious tilts and comas by iterating with the translation stage and relative intensities are compared to find the diffraction limited area.

4.3.2 Resolution

The resolution measurement is done for 766 nm in, however this time in dependence of the aperture stop radius in Figure 4.12.

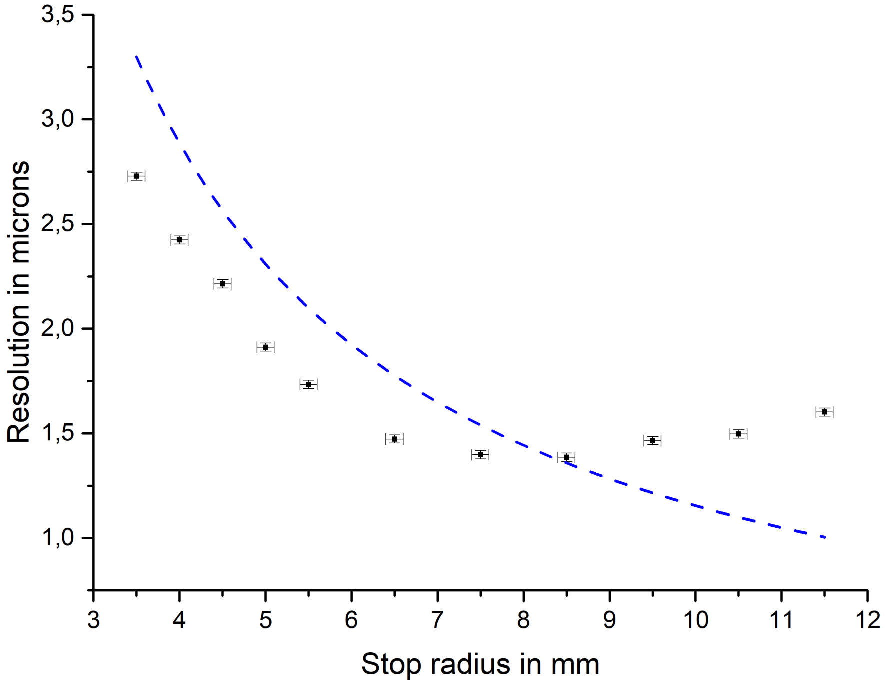

Figure 4.12: The graph shows the measured FHWM resolution versus aperture stop radius. The stop radius starting at 11,5 mm is decreased by 2 mm steps and several measurements are taken at each position. The errors are the averaged fit errors from each Gaussian fit, as it was done in figure 4.6. The dashed line marks the theoretical airy disk radius for the according to equation (2.19).

The measurements in figure 4.12 are basically an extended measurement from figure 4.6, where each measurement point is the average of 10 measurements for the respective stop diameter. This graph shows the behaviour of the experimental resolution which is decreasing for an increasing stop diameter, until at some point spherical aberrations get dominant enough to cause a broadening of the FWHM and thereby worsen the resolution. In contrast, the theoretical resolution limit according to the Rayleigh criterion is continously decreasing for an increasing stop diameter. The graph suggests a stop diameter between 15 mm and 17 mm is favourable for the best possible resolution while still being diffraction limited.

4.3.3 Strehl ratio

The wavefront error is retrieved for the SNOM measurement as well. It is of interset, whether or not rebuilding the tube and having the new light source not in the exact same spot as before still provides the same results. This time, 10 optimization runs are performed with 500 iterations each, two images per iteration. The averaged results of the Zernike coefficients are presented in Figure 4.13

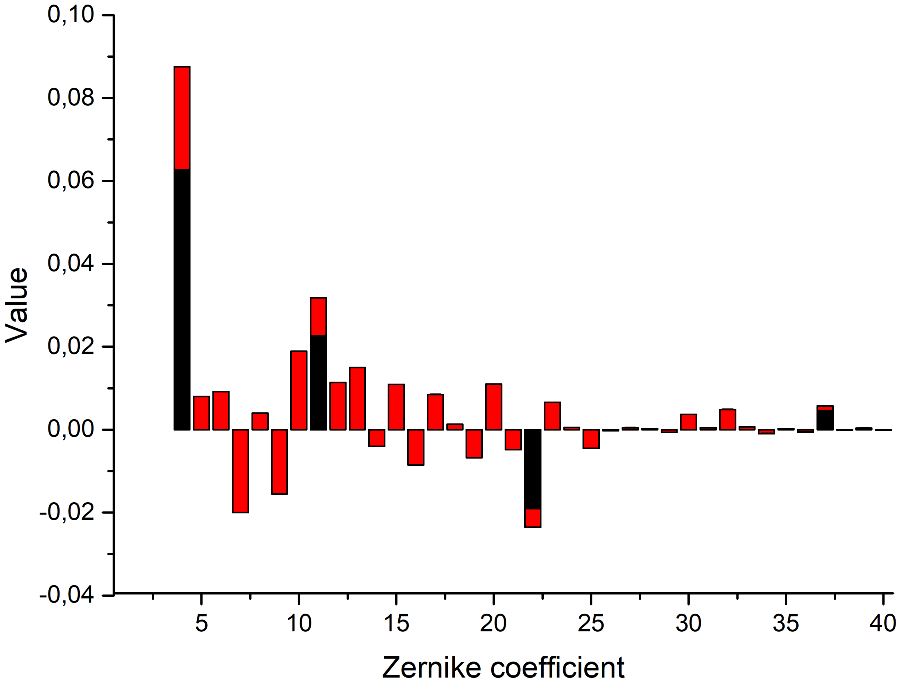

Figure 4.13: Zernike polynomials from phase retrieval for 766 nm. The black bars represent the theoretical expected values and red the retrieved ones.

With the coefficients shown in Figure 4.13, the wavefront error and Strehl ratio is calculated

$$W_{RMS}^{766,SNOM} = 0,0557(8), \quad S^{766,SNOM} = 0,88(1).$$

The value is within its 1σ deviation of the pinhole measurement. At first glance, when comparing the Zernike values, the fifth and sixth term dropped the most, corresponding to a lower astigmatism. This could relate to either the front lens or the back achromatic lens not being aligned the same way as in the pinhole measurement since they were removed and put back in a couple of times. Or, it is simply of statistical nature since less optimizations are made, thus a larger error.

4.4 Measurement discussion

The measured values are compared to the predicted values in table 4.1. Since the aperture spot in the experimental setup was chosen to be 17 mm, all values are compared to a the same stop diameter in the simulation.

Table 4.1: Comparison between measurement results and ray tracing estimates.

Parameter	Simulation results	Experimental results
Magnification	35,1	34,4(4)
Resolution limit	1,19 μm for 671 nm 1,36 μm for 766 nm	1,43(1) μm for 671 nm 1,55(1) μm for 766 nm
Strehl ratio	0,935 for 671 nm 0,943 for 766 nm	0,894(3) for 671 nm 0,878(5) for 766 nm
Field of view	220 μm for 671 nm 220 μm for 766 nm	110 μm for 671 nm 90 μm for 766 nm
Focal shift (image space)	400 μm	370(10) μm

The measured magnification is in good agreement, within 2σ, of the expected value. The measured resolution is roughly 20% larger than the Rayleigh limit which is most likely due to spherical aberrations being higher than expected from the simulation, hence a smaller aperture stop is chosen to compensate for those. Overall the system shows diffraction limited performance over a sufficiently large field of view, even though the values are not a good as the simulation suggested. This is not entirely unexpected since four of the lenses were commercial lenses with larger uncertainties in their radii and thickness compared to more expensive custom lenses. The chromatic focal shift is within the maximum predicted focal shift range. The reason for giving a range in the predicted value instead of an exact value, is because moving the entry lens has an impact on the chromatic performance, according to the simulation. Ideally it should be kept in its designed position to avoid losing achromatic performance.

The Zernike polynomials extracted from phase retrieval indicate where the aberrations come from. Figure 4.14 shows their shape. According to the model, the j=4 coefficient or defocus is dominant, which arises from the fact that the design features achromatic performance. As phase retrieval was performed for each wavelength separately, the measured value should be taken with a grain of salt. Astigmatism and coma are most likely enhanced by improper alignment of the pinhole with the objective. Apart from that, surface tilt with respect to each other inside the lens tube would also cause these types of aberrations. Spherical aberrations are subject to lens spacings and can be enhanced by uncertainties in lens thickness. Higher order terms, as well as tre- and pentafoil, can not be specified to a simple origin, but are likely a result of uncertainties in lens parameters, such as thickness and diameter. The cut-off at 40 polynomials was chosen because earlier runs have shown that higher order terms up to 80 made up less than 1% of the total wavefront error.

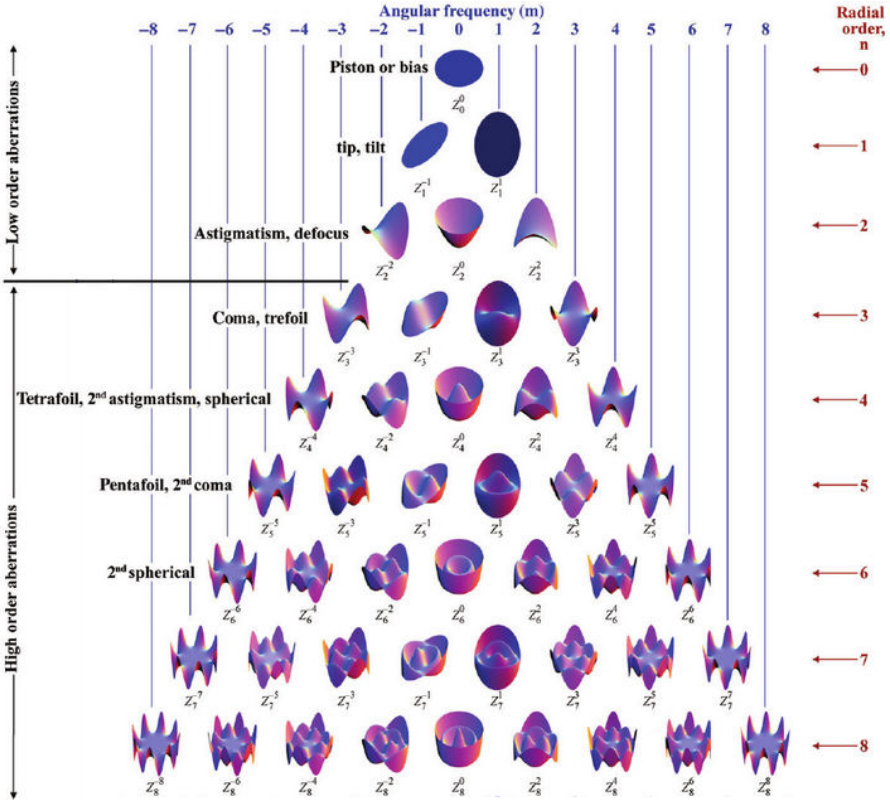

Figure 4.14: Plots of the first 45 Zernike polynomials. Image taken from [35].

5 Summary and Outlook

In this work, the prerequisites for designing an objective to image ultracold quantum gases were discussed and its experimental testing was done and compared to simulation results. It is remarkable, that given all the boundary conditions such as being able to image through a vacuum glass cell, having achromatic performance and a resolution far below 2 micron, such an objective could be built almost entirely from off-the-shelve standard lenses for little cost. The results of the ray tracing software also seem to be reliable and are thus an important asset in the design process.

In the next step, the objective could be implemented into the experiment and replace the x4 magnification system, as mentioned in section 1.4. As both wavelengths are intended to be imaged on separate CCD cameras, a polarizing beamsplitter would have to be placed in the infinite conjugate plane and then two imaging lenses in each of the arms to form the image on the CCD chips. The PBS should ideally not add an additional wavefront error in the infinite conjugate plane, as it just adds a constant phase delay as discussed in section 2.3.3. The upgraded imaging system will hopefully contribute to allow a deeper analysis of the ongoing research in the FeLiKx group as future studies might include investigating the two dimensional character of the interface between the bosonic and the fermioninc layer [22].

The phase retrieval algorithm used has yet seen limited application in microscopy experiments, apart from [24]. Even though the results agree fairly well with the predicted wavefront error from the OpticStudio simulation, it would be interesting to compare these results with the wavefront error retrieved by other, more common, means for example with a Shack-Hartmann wavefront sensor [36].

Bibliography

[1] Lipson, A.: *Optical Physics*. Cambridge University Press, 2010

[2] *Kapitel* Chapter 6. In: Hung, Chen-Lung ; Chin, Cheng: *Imaging of Atomic Quantum Gases*, S. 101–120

[3] M.H. Anderson, M.R. Matthews C.E. Wieman E.A. C. J.R. Ensher E. J.R. Ensher: Observation of Bose-Einstein Condensation in a Dilute Atomic Vapor. In: *Science* 269 (1995), Juli, S. 198–201

[4] Tarik Yefsah, Lauriane Chomaz Kenneth J. Günter Jean D. Rémi Desbuquois D. Rémi Desbuquois: Exploring the thermodynamics of a two-dimensional Bose gas. In: *arXiv* (2011), Nr. arXiv:1106.0188

[5] Baranov, M. A. ; Dalmonte, M. ; Pupillo, G. ; Zoller, P.: Condensed Matter Theory of Dipolar Quantum Gases. In: *Chemical Reviews* 112 (2012), Nr. 9, 5012-5061. `http://dx.doi.org/10.1021/cr2003568`. – DOI 10.1021/cr2003568. – PMID: 22877362

[6] *Kapitel* Chapter 7. In: Hung, Chen-Lung ; Chin, Cheng: *Imaging of Atomic Quantum Gases*, S. 121–143

[7] Bakr, Waseem S. ; Gillen, Jonathon I. ; Peng, Amy ; Fölling, Simon ; Greiner, Markus: A quantum gas microscope for detecting single atoms in a Hubbard-regime optical lattice. In: *Nature* 462 (2009), November, 74. `https://doi.org/10.1038/nature08482`

[8] Maxwell F. Parsons, Anton Mazurenko Christie S. Chiu Widagdo Setiawan Katherine Wooley-Brown Sebastian Blatt Markus G. Florian Huber H. Florian Huber: Site-resolved Imaging of Fermionic Lithium-6 in an Optical Lattice. In: *arXiv* (2015), Nr. arXiv:1504.04397

[9] Haller, Elmar ; Hudson, James ; Kelly, Andrew ; Cotta, Dylan A. ; Peaudecerf, Bruno ; Bruce, Graham D. ; Kuhr, Stefan: Single-atom imaging of fermions in a quantum-gas microscope. In: *Nature Physics* 11 (2015), Juli, 738. `https://doi.org/10.1038/nphys3403`

[10] Lawrence W. Cheuk, Melih Okan Thomas Gersdorf Vinay V. Ramasesh Waseem S. Bakr Thomas Lompe Martin W. Z. Matthew A. Nichols N. Matthew A. Nichols: A Quantum Gas Microscope for Fermionic Atoms. In: *arXiv* (2015), Nr. arXiv:1503.02648

[11] G. J. A. Edge, D. Jervis D. C. McKay R. Day S. Trotzky J. H. T. R. Anderson A. R. Anderson: Imaging and addressing of individual fermionic atoms in an optical lattice. In: *arXiv* (2015), Nr. arXiv:1510.04744

[12] Ahmed Omran, Timon Hilker Katharina Kleinlein Guillaume Salomon Immanuel Bloch Christian G. Martin Boll B. Martin Boll: Microscopic Observation of Pauli Blocking in Degenerate Fermionic Lattice Gases. In: *arXiv* (2015), Nr. arXiv:1510.04599

[13] Sherson, Jacob F. ; Weitenberg, Christof ; Endres, Manuel ; Cheneau, Marc ; Bloch, Immanuel ; Kuhr, Stefan: Single-atom-resolved fluorescence imaging of an atomic Mott insulator. In: *Nature* 467 (2010), August, 68. `https://doi.org/10.1038/nature09378`

[14] Ryuta Yamamoto, Takuma Kuno Kohei Kato Yoshiro T. Jun Kobayashi K. Jun Kobayashi: An ytterbium quantum gas microscope with narrow-line laser cooling. In: *arXiv* (2015), Nr. arXiv:1509.03233

[15] Miranda, Martin S.: *Quantum gas microscope forytterbium atoms*, Tokyo Institute of Technology, Diss., 2016

[16] W. S. Bakr, M. E. Tai R. Ma J. Simon J. I. Gillen S. Fölling L. Pollet M. G. A. Peng P. A. Peng: Probing the Superfluid–to–Mott Insulator Transition at the Single-Atom Level. In: *Science* (2010)

[17] Simon, Jonathan ; Bakr, Waseem S. ; Ma, Ruichao ; Tai, M. E. ; Preiss, Philipp M. ; Greiner, Markus: Quantum simulation of antiferromagnetic spin chains in an optical lattice. In: *Nature* 472 (2011), April, 307. `https://doi.org/10.1038/nature09994`

[18] Philipp M. Preiss, M. Eric Tai Alexander Lukin Matthew Rispoli Philip Zupancic Yoav Lahin Rajibul Islam Markus G. Ruichao Ma M. Ruichao Ma: Strongly correlated quantum walks in optical lattices. In: *Science* 347 (2015), S. 1229–1233

[19] M. Endres, T. Fukuhara C. Weitenberg P. Schauß C. Gross L. Mazza M. C. Bañuls L. Pollet I. Bloch S. K. M. Cheneau C. M. Cheneau: Observation of Correlated Particle-Hole Pairs and String Order in Low-Dimensional Mott Insulators. In: *Science* 334 (2011), S. 200–203

[20] Maxwell F. Parsons, Christie S. Chiu Geoffrey Ji Daniel Greif Markus G. Anton Mazurenko M. Anton Mazurenko: Site-resolved measurement of the spin-correlation function in the Fermi-Hubbard model. In: *Science* 353 (2016), S. 1253–1256

[21] Lous, Rhianne: *Tunable Bose-Fermi and Fermi-Fermi Mixtures of Potassium and Lithium*, University of Innsbruck, Diss., 2018

[22] Lous, Rianne S. ; Fritsche, Isabella ; Jag, Michael ; Lehmann, Fabian ; Kirilov, Emil ; Huang, Bo ; Grimm, Rudolf: Probing the Interface of a Phase-Separated State in a Repulsive Bose-Fermi Mixture. In: *Phys. Rev. Lett.* 120 (2018), Jun, 243403. `http://dx.doi.org/10.1103/PhysRevLett.120.243403`. – DOI 10.1103/PhysRevLett.120.243403

[23] Brady, Gregory R. ; Fienup, James R.: Nonlinear optimization algorithm for retrieving the full complex pupil function. In: *Opt. Express* 14 (2006), Jan, Nr. 2, 474–486. `http://dx.doi.org/10.1364/OPEX.14.000474`. – DOI 10.1364/OPEX.14.000474

[24] Marszalek, Mirsolaw: *Assembly and testing of an objective lens design for imaging ultracold quantum gases*, University of Innsbruck, Diplomarbeit, 2017

[25] Geary, Joseph M.: *Introduction to lens desgin.* Willmann-Bell, Inc, 2002

[26] Mahajan, Virendra N.: *Optical Imaging and Aberrations, part 1, ray geometrical optics.* SPIE, 1998

[27] Goodman, J. W.: *Introduction to Fourier Optics.* McGraw-Hill, 1996

[28] Mahajan, Virendra N.: *Optical Imaging and Aberrations, part 3, wavefront analysis.* SPIE, 2013

[29] Tichenor, D. A. ; Goodman, J. W.: Coherent Transfer Function. In: *J. Opt. Soc. Am.* 62 (1972), Nr. 2, S. 293–295

[30] Wilson, R. G.: Wavefront-error evaluation by mathematical analysis of experimental Foucault-test data. In: *Appl. Opt.* 14 (1975), Sep, Nr. 9, 2286–2297. `http://dx.doi.org/10.1364/AO.14.002286`. – DOI 10.1364/AO.14.002286

[31] Schwider, J. ; Burow, R. ; Elssner, K.-E. ; Grzanna, J. ; Spolaczyk, R. ; Merkel, K.: Digital wave-front measuring interferometry: some systematic error sources. In: *Appl. Opt.* 22 (1983), Nov, Nr. 21, 3421–3432. `http://dx.doi.org/10.1364/AO.22.003421`. – DOI 10.1364/AO.22.003421

[32] Mahajan, Virendra N.: *Optical imaging and Aberrations, part 2, wave diffraction optics.* SPIE, 2011

[33] Jenkins, Harvey E. Francis A.; White W. Francis A.; White ; Grall, Shirley (Hrsg.): *Fundamentals of Optics.* McGraw-Hill Custom Publishing, 1976

[34] O. Shvedchenko, D ; Suvorova, Elena: New method of automated statistical analysis of polymer-stabilized metal nanoparticles in electron microscopy images. In: *Crystallography Reports* 62 (2017), 09, S. 802–808. `http://dx.doi.org/10.1134/S1063774517050200`. – DOI 10.1134/S1063774517050200

[35] Lakshminarayanan, Vasudevan ; Fleck, Andre: Zernike polynomials A guide. In: *Journal of Modern Optics* 58 (2011), S. 1678

[36] Lee, Jin-Seok ; Yang, Ho-Soon ; Hahn, Jae-Won: Wavefront error measurement of high-numerical-aperture optics with a Shack-Hartmann sensor and a point source. In: *Appl. Opt.* 46 (2007), Mar, Nr. 9, 1411–1415. `http://dx.doi.org/10.1364/AO.46.001411`. – DOI 10.1364/AO.46.001411